Multifunctional High Entropy Alloys Enabled by Severe Lattice Distortion

Wang, Hang; He, Quanfeng; Gao, Xiang; Shang, Yinghui; Zhu, Wenqing; Zhao, Weijiang; Chen, Zhaoqi; Gong, Hao; Yang, Yong

Published in:
Advanced Materials

Published: 25/04/2024

Document Version:
Post-print, also known as Accepted Author Manuscript, Peer-reviewed or Author Final version

Published version (DOI):
10.1002/adma.202305453

Publication details:
Wang, H., He, Q., Gao, X., Shang, Y., Zhu, W., Zhao, W., Chen, Z., Gong, H., & Yang, Y. (2024). Multifunctional High Entropy Alloys Enabled by Severe Lattice Distortion. *Advanced Materials*, *36*(17), Article 2305453. https://doi.org/10.1002/adma.202305453

Multifunctional High Entropy Alloy Enabled by Severe Lattice Distortion

Hang Wang[1], Quanfeng He[1,2], Xiang Gao[1], Yinghui Shang[1,3], Wenqing Zhu[1,4], Weijiang Zhao[1,5], Zhaoqi Chen[1], Hao Gong[1], Yong Yang[1,6,*]

[1.] Department of Mechanical Engineering, College of Engineering, City University of Hong Kong, Kowloon Tong, Kowloon, Hong Kong, China

[2.] Institute of Materials Modification and Modeling, School of Materials Science and Engineering, Shanghai Jiao Tong University, Shanghai, 200240, China

[3.] City University of Hong Kong (Dongguan), Dongguan, Guangdong, 523000, China

[4.] State Key Laboratory for Turbulence and Complex System, Department of Mechanics and Engineering Science, College of Engineering, Peking University, Beijing 100871, China.

[5.] Powder Metallurgy Research Institute, Central South University, Changsha, Hunan, 410083, China

[6.] Department of Materials Science and Engineering, College of Engineering, City University of Hong Kong, Kowloon Tong, Kowloon, Hong Kong, China

*Corresponding author. yonyang@cityu.edu.hk

Abstract

Since 2004, the design of high entropy alloys (HEAs) has generated significant interest within the materials science community due to their exceptional structural and functional properties. By incorporating multiple principal elements into a common lattice, it is possible to create a single-phase crystal with a highly distorted lattice. This unique feature enables HEAs to offer a promising combination of mechanical and physical properties that are not typically observed in conventional alloys. In this article, we provide an extensive overview of multifunctional HEAs that exhibit severe lattice distortion, covering the theoretical models that were developed to understand lattice distortion, the experimental and computational methods employed to characterize lattice distortion, and most importantly, the impact of severe lattice distortion on the mechanical, physical and electrochemical properties of HEAs. Through this review, we hope to stimulate further research into the study of distorted lattices in crystalline solids.

Keywords: Lattice distortion, high entropy alloys, multifunctionality

1. Introduction

Throughout history, human civilization has been greatly influenced by the discovery and development of new materials. Historical epochs have been named after the most significant materials that were developed and widely used, such as the Bronze Age and Iron Age.[1–4] Traditionally, the development of metals has been based on one or two principal metallic elements with minor alloying elements used for property enhancement. For example, the addition of zinc to copper created bronze, which had higher strength and better ductility.[5] Similarly, the addition of carbon and chromium to iron produced stainless steel, which had higher strength and better corrosion resistance.[6,7] This traditional paradigm for alloy design has been successfully followed for many useful alloys over the past millennia.[8] However, in 2004, Yeh et al.[9] and Cantor et al.[10] proposed a new alloy design paradigm that involves mixing five or more principal elements in an equimolar or near-equimolar ratio. These multi-principal element alloys (MPEAs) or high entropy alloys (HEAs) have no unique base elements,[11,12] but exhibit fascinating mechanical, physical, and electrochemical properties.[11–14] Furthermore, Yeh et al.[15,16] proposed four "core effects" for HEAs, namely the high entropy effect, sluggish diffusion, lattice distortion and chemical "cocktail" effect, which have been extensively invoked to rationalize the excellent properties of HEAs in the literature.[17–21] Among these "core effects", lattice distortion has been considered as the fundamental factor contributing to the impressive properties of HEAs.[19–21]

In the field of materials science, it is widely agreed that alloying different sized elements into a common lattice results in a distorted lattice, which displaces the constituent atoms from their ideal positions, giving rise to the lattice distortion effect.[16,22,23] The lattice distortion effect induces a highly fluctuating elastic stress/strain field in HEAs, which has been demonstrated to be vital in dislocation behavior.[24,25] Additionally, lattice distortion helps stabilize a thermodynamically nonequilibrium state, which reduces the energy barrier for active species such as electrons and ions.[26,27] Consequently, HEAs with a distorted lattice exhibit more impressive multifunctional properties than conventional alloys, such as super elasticity,[28]

outstanding strength and plasticity,[29–31] high thermoelectric performance[32], distinctive irradiation resistance[33,34] and promising catalytic efficiency.[35,36]

The unique combination of mechanical and physical properties in HEAs expands their application scenarios and makes them more versatile than conventional alloys. For example, conventional ferromagnetic Fe-Ni and Fe-Co-based Elinvar alloys cannot function properly in a magnetic environment due to their Elinvar effect being closely related to the magnetic phase transition.[37] However, a newly developed B2 $(CoNi)_{50}(TiZrHf)_{50}$ HEA exhibits a strong Elinvar effect of non-magnetic origin due to severe lattice distortion,[28] making them applicable in complex and extreme environments. The FCC Cantor alloy (FeCoNiCrMn) is also renowned for its combination of high fracture toughness at cryogenic temperatures[38] and irradiation resistance.[34,39] These findings are intriguing and call for more attention to the development of multifunctional HEAs. In this article, we will review the thermodynamics and micromechanics that govern lattice distortion in both conventional alloys and HEAs together with the experimental and computational characterization of lattice distortion in HEAs. Specifically, we will discuss and exemplify the effects of lattice distortion on the mechanical properties, transport properties, irradiation resistance, and catalytic properties of HEAs.

2. The Concept of Lattice Distortion

Lattice Distortion as Heterogeneous Elastic Strain Field The concept of lattice distortion has a well-established history in physical metallurgy. As depicted in **Figs. 1(a-b)**, the incorporation of solute atoms into a metal results in local lattice distortion due to the difference in atomic size and elastic modulus between the solute and solvent atoms (note that the atomic size data for various elements can be found in Ref.[40]). From a thermodynamic viewpoint, local lattice distortion results from the minimization of the Gibbs free energy of the alloy.[41,42] In the case of conventional dilute solid solutions, the field of elastic atomic displacement u_i, which characterizes the local distortion, is obtained from the classic Eshelby theory[43,44]

$$u_i = \frac{e_{jk}^{\infty}}{8\pi(1-\nu)} \int_V g_{ijk} \frac{dv}{r^2} \quad (1)$$

where e_{jk}^{∞} denote a remote finite strain; v is the Poisson's ratio; r is the distance of the solute atom to the point of interest, and g_{ijk} is a function of the coordinates of the point of interest relative to the solute atom. As per **Eq. (1)**, lattice distortion rises with the Poisson ratio, with a minimum being reached at v = -1 and a maximum at v = 0.5. Nonetheless, the influence of lattice distortion wanes briskly with a rise in distance from the dilute atom. In a region far from the solute atom, **Eq. (1)** becomes to $u_i(x) \propto \frac{1}{r^2}$.

The existence of elastic fields [**Eq. (1)**] makes it challenging for defects, such as dislocations, to move since elastic interactions can hinder their motion efficiently. As per Refs.[45–47], the size and modulus difference between the solute and solvent atoms dictate the elastic interaction. For dilute solutions without solute-solute interactions, Fleischer[48,49] derived the critical stress τ_c at which a dislocation can surmount solute pinning $\tau_c = \frac{f_0^{3/2} c^{1/2}}{b(2T_d)^{1/2}}$ where b is the Burger's vector; f_0 is a function of size and modulus difference; c is the solute concentration and T_d is the dislocation line tension. In contrast, Labusch[50] considered elastic interactions among neighboring solutes and derived the critical de-pinning stress as $\tau_c = C\frac{f_0^{4/3} w^{1/3} c^{2/3}}{b(4T_d)^{1/3}}$ where w is the range of the interaction force and C is a numerical constant. Here we note that the Labusch model can operate throughout the concentration range, making it much more versatile than the Fleischer model that only applies to dilute solid solutions.[14,51]

The mean field approach, which includes Eshelby theory[52] and Labusch model[50], can accurately describe lattice distortion and its associated elastic stress fields around solute atoms in conventional alloys. However, extending this technique to concentrated solutions proves to be challenging, particularly when solute atoms become indistinguishable from the solvent atoms, as depicted in **Fig. 1(c).** At this point, atoms must relocate away from their ideal lattice positions, creating a severe lattice distortion and a highly fluctuating elastic stress field that seemingly elevates the total energy of the entire lattice. This situation prompts an intriguing question: why and how can the lattice be severely distorted if such an adjustment can significantly increase its energy? In response to this inquiry, one may first assume that atomic

displacement does not occur even when different-sized atoms are inserted into a common lattice. In such instances, it is conceivable that the constituent atoms become either stretched-out or squeezed-in, thereby fitting into the lattice structure. If the atomic size change is assumed to be purely elastic, Ye et al.[53] derived the elastic strain ε_i experienced by the i^{th} element with the concentration c_i, which corresponds to the average elastic strain $\langle\varepsilon\rangle = \sum_{j=1}^{n} c_j\varepsilon_j = 0$, and the variability of the elastic strain field as $\varepsilon_{RMS} = \sqrt{\sum c_i\varepsilon_i^2}$, which demonstrates a connection with the elastic energy accumulation in the lattice structure.[53] This metric ε_{RMS} may also function as an indicator for evaluating the stability of such structures.[11,53,54]

When atoms are permitted to deviate from their ideal lattice positions, their movement could cause partial relaxation of the elastic energy accumulation due to atomic size changes, resulting in a reduction of E_1 (**Fig. 1(d)**). Simultaneously, the atomic displacements also alter the lattice shape, thereby increasing the elastic energy by an amount of E_2 (**Fig. 1(d)**). Essentially, lattice distortion is favorable from an energy standpoint when $E_1 > E_2$. According to Ref.[23], lattice distortion is influenced not only by atomic size differences but also by the Poison's ratio (v). Similar to lattice distortion in conventional alloys strengthened by solute, lattice distortion in high entropy materials also rises with the Poisson ratio according to the model of Ye et al.[23]

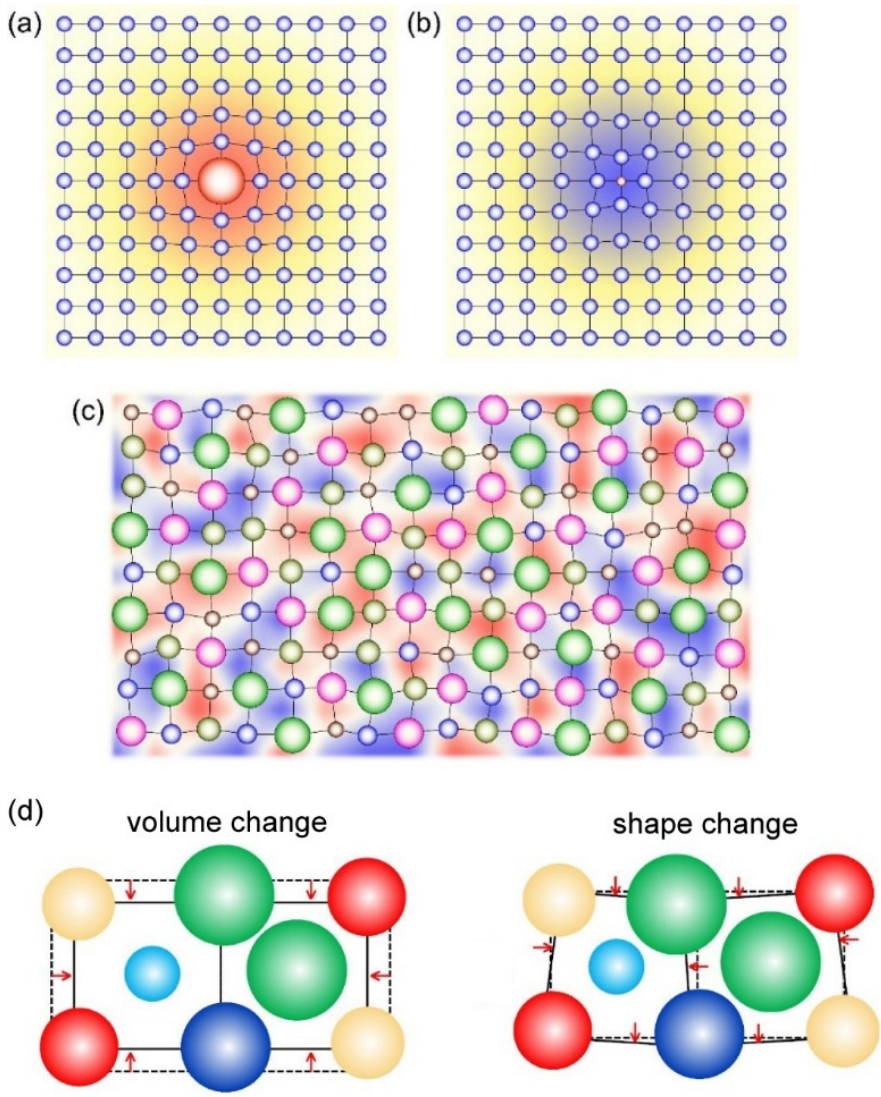

Figure 1. Schematic plot of local distorted lattice in (a) conventional solid solution alloys where the solute atom is larger than solvent atom, (b) conventional solid solution alloys where the solute atom is smaller than solvent atom, and (c) high entropy alloys. (d) The schematic illustration of a lattice experiencing volume change and shape change in a multicomponent alloy system.

Lattice Distortion as "Misfit Volumes" Aside from the elastic approach proposed by Ye et al.[23,53] , which considers lattice distortion as the result of minimizing elastic energy. Another approach is the phenomenological model that treats each constituent atom in HEAs as a "solute" atom embedded in an average "matrix"[55–57]. The local atomic misfit volume is characterized

in the latter approach, and defined as $\Delta V_n = \sum_m c_m < \Delta V^{n/m} >$, where $< \Delta V^{n/m} >$ represents the average volume change caused by replacing one type-*m* atom with type-*n* atom.[55–57] The atomic misfit volume leads to deviation from perfect lattice sites and eventually results in lattice distortion. To quantify this distortion, Nöhring et al.[58] proposed the root mean square displacement of atoms (u_{rms}) from the exact lattice positions $u_{rms} \approx \sqrt{\sum_p^3 \sum_m^{N_T} c_m \sum_i^N \left(u_{i,p}^{(m)}\right)^2}$ where N_T is total number of constituent elements; N is the total number of lattice sites and $u_{i,p}^{(m)}$ is the *p*-component of misfit-induced displacement vector at lattice site *i* generated by type-*m* solute, as illustrated in **Figs. 2(a-b)**. Furthermore, Nöhring et al.[58] demonstrated a correlation between u_{rms} and the misfit volume parameter $\delta = \sqrt{\sum_n c_n \Delta V_n^2}/b^3$ through the equation $u_{rms} = k \cdot b \cdot \delta^{4/3}$ by following the plasticity strengthening theories and the "average alloy" potential developed by Varvenne et al.[55,59,60], where *b* is the Burgers vector and *k* is a coefficient that depends on the compositions of the HEAs (e.g., $k \approx 1.2$ for Cr-Fe-Ni and $k \approx 0.7$ for Mo-Nb-V).

Lattice Distortion as Atomic Size/Angle Difference The averaged atomic size difference in HEAs was quantified by Zhang et al.[61] in 2008 using an empirical parameter $\delta = \sqrt{\sum_{i=1}^n c_i \left(1 - r_i / \sum_{j=1}^n c_j r_j\right)^2}$, where *n* is the number of constituent elements; c_i and c_j are the atomic percentage of the i^{th} and j^{th} elements respectively; r_i and r_j represent the atomic size of the i^{th} and j^{th} elements respectively. Wang et al.[62] developed two geometric parameters that consider the difference of solid angles around the largest and smallest atoms in HEAs: $\omega_L = 1 - \sqrt{1 - (\overline{r})^2/(r_L + \overline{r})^2}$ and $\omega_S = 1 - \sqrt{1 - (\overline{r})^2/(r_S + \overline{r})^2}$ (see **Figs. 2(c-d)**), where ω_L and ω_S are solid angles around the largest and smallest atoms respectively; $\overline{r}$ is the averaged atomic radius; r_L and r_S are the atomic radius of the largest and smallest atoms respectively. While these empirical parameters only consider atomic size effect with an assumption that atoms behave as rigid 'balls', they serve as the first indicator of possible lattice distortion in

HEAs, where larger values indicate severe lattice distortion.[11]

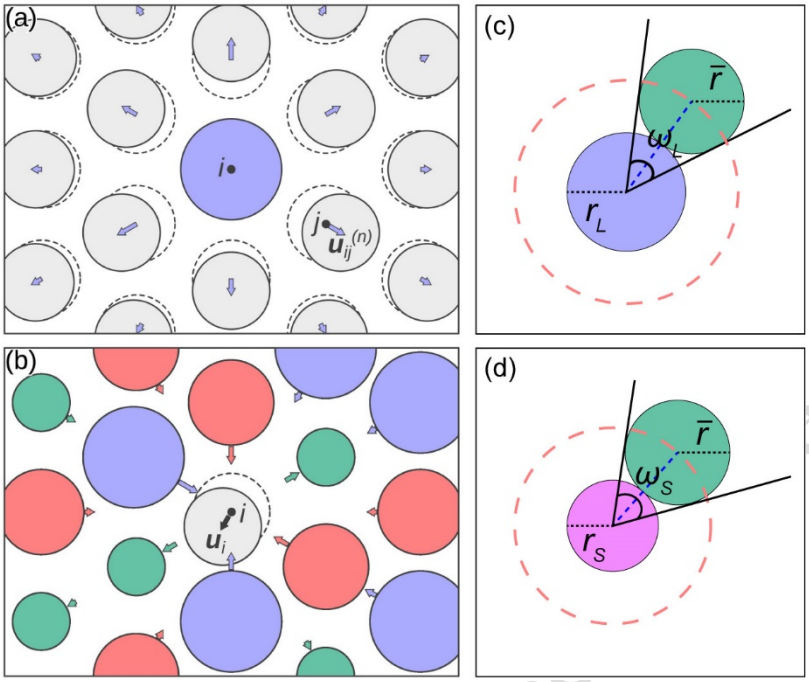

Figure 2. (a) Displacement field created by a single solute in the average "matrix". (b) Displacement of an atom at position *i* created by the sum of the displacements at site *i* generated by all of the surrounding solutes on sites *j*. Reproduced with permission.[58] The sketch of the solid angle around (c) the largest atom and (d) the smallest atom. $\bar{r}$ is the average atomic radius. Reproduced with permission.[62]

Lattice Distortion versus Chemical Short-Range Ordering/Demixing Excessive lattice distortion in random solid solutions can result in phase transitions or amorphization, indicating that lattice distortion may promote chemical ordering or elemental segregation, as discussed in Ref [53]. For random alloys with significant atomic size misfit, severely distorted lattices are favored in theory,[23,53] as shown in **Fig. 3**. However, achieving complete chemical randomness is only feasible at very high temperatures,[2] and at intermediate or low temperatures, chemical short-range ordering (CSRO) is almost inevitable in HEAs after thermal annealing. The formation of CSRO may release some of the elastic energies caused by local lattice variations, making it more thermodynamically favorable, as depicted in **Fig. 3**. However, lattice distortion in real HEAs can also hinder the kinetics of CSRO formation. For instance, He et al.[63]

demonstrated that the formation of CSRO in FCC FeCoNiCr after thermal annealing was difficult due to lattice distortion. Despite the growing interest in CSRO studies,[64–68] the relationship between CSRO and lattice distortion remains an open issue.[69,70]

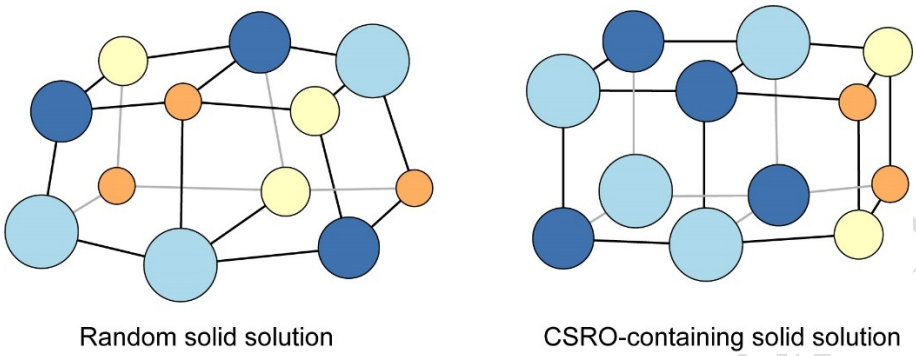

Figure 3. Schematic plot of a random solid solution with severe lattice distortion in comparison to the CSRO-containing solid solution with less lattice distortion.

In summary, while empirical parameters such as atomic size/angle difference,[61,62] have been widely employed as indicators for the degree of lattice distortion in HEAs, it is important to note that lattice distortion is physically linked to a heterogeneous strain field. This field is generated by the contraction/dilation of atomic volumes and the deviation of atoms from their positions in an ideal lattice. Moreover, according to previous works,[23] the average strains (either normal or shear) associated with lattice distortion in HEAs is negligibly small. Therefore, fundamentally, lattice distortion is characterized by the fluctuation or variation of lattice strains, which can be also connected to the variation of elastic energy[23,53] and misfit volumes.[55–57] Following this reasoning, a "severely" distorted lattice could be interpreted as a lattice with a highly fluctuating strain field. According to the Lindeman criterion,[71] the maximum variation of the lattice strain field, as quantified by the standard deviation of the corresponding normal strains, can reach approximately 10% before the distorted crystal becomes thermodynamically unstable.

3. Characterization of Lattice Distortion

In the early literature of HEAs, X-ray diffraction (XRD) was once used to characterize lattice distortion, which was interpreted as peak broadening in the XRD profile.[17,72] However, caution must be taken during sample preparation for XRD measurement to minimize the local lattice strain caused by defects such as dislocations.[73] Because of the minimal impact of lattice distortion on the interplanar spacing of a pristine lattice[23,53,73] and some unavoidable factors, such as sample absorption and electron cloud scattering, it is indeed challenging to accurately determine intrinsic lattice strain using XRD. In comparison to XRD, high-energy synchrotron X-ray diffraction and neutron scattering can more effectively assess atomic-scale lattice distortion.[74–79] Total scattering data from these methods can produce the atomic pair distribution function (PDF), which offers information on inter-atomic positions with real space accuracy to within a thousandth of an angstrom through Fourier transformation.[80] The reduced PDF *G(r)* can be derived from the experimentally obtained structure function[81–83] $G(r) = \frac{2}{\pi}\int Q[S(Q)-1]sin(Qr)dQ$, where r is the interatomic distance; $Q = 4\pi sin\theta/\lambda$ is the scattering vector in which θ is half of the scattering angle and λ is the X-ray or neutron wavelength. By comparison, *G(r)* for a perfect crystalline structure can be simply expressed as[82] $G_c^r = \frac{1}{r}\sum_{i,j}\left[\frac{b_i b_j}{\langle b\rangle^2}\delta(r-r_{ij})\right] - 4\pi r\rho_0$, where b_i and b_j are the scattering length of atom *i* and *j*, respectively; r_{ij} is the distance between atom *i* and *j*; $\langle b\rangle$ is the average scattering length; $\delta(r-r_{ij})$ is the delta function and ρ_0 is the average atom number density. In principle, any local structural variations can be derived through the difference between $G(r)$ and G_c^r. **Figures 4(a-b)** demonstrate the reduced PDF *G(r)* of a variety of BCC refractory HEAs. In contrast to the sharp PDF peaks in the alloys without Zr and Hf, the Zr- and/or Hf-containing alloys clearly exhibit a single broad PDF peak across the first and second atomic shells (**Fig. 4(b)**), suggestive of strong lattice distortion.[79]

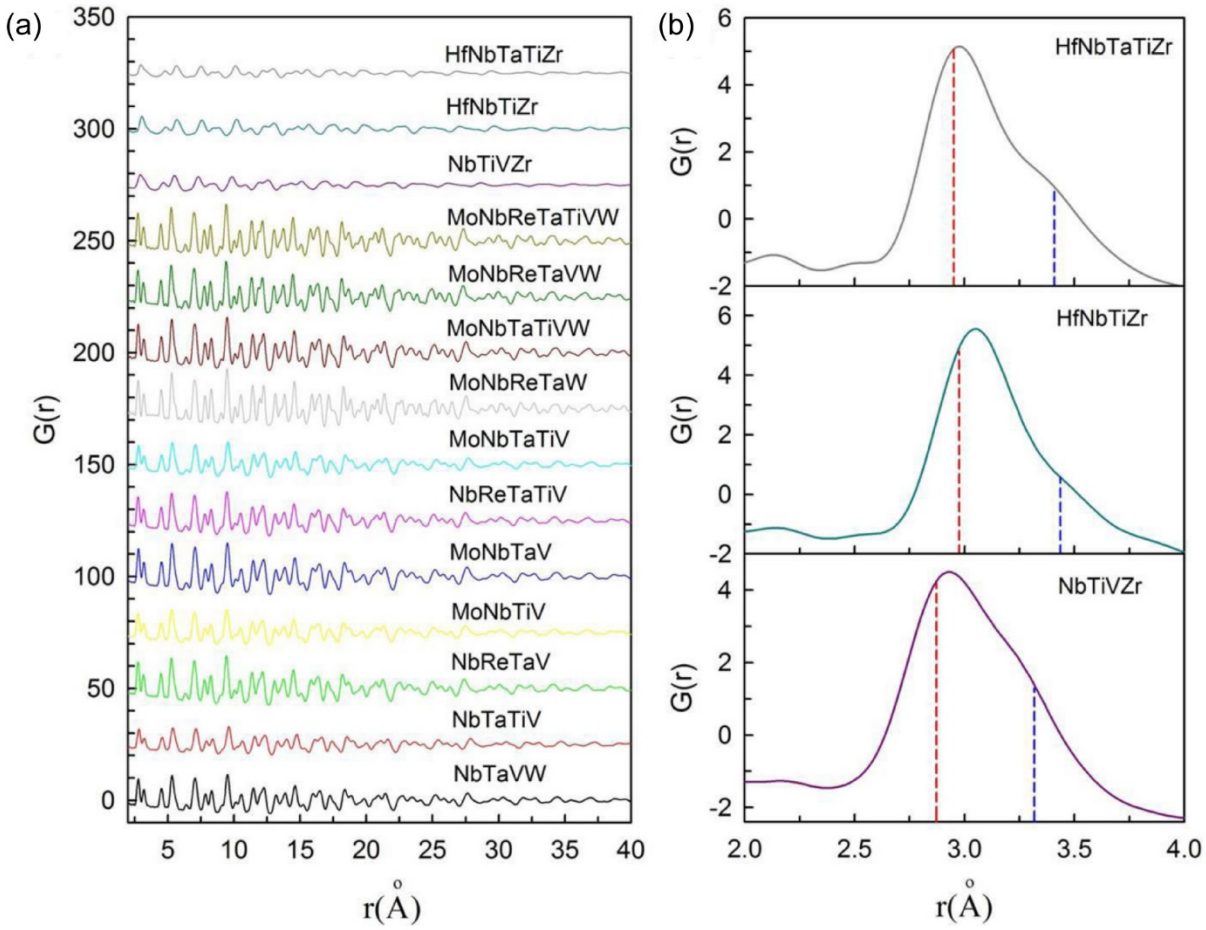

Figure 4. (a) The reduced PDFs of refractory alloys. (b) The enlarged views of the first and second atomic shells for HfNbTaTiZr, HfNbTiZr and NbTiVZr alloys. The red and blue dashed lines indicate the ideal positions of the first and second shells respectively. Reproduced with permission.[79]

State-of-the-art transmission electron microscopy (TEM) techniques have been employed as an alternative method to assess lattice strain in various materials.[84–89] Achieving a spatial resolution of at least 0.001 nm is required to resolve 1% lattice strain over a lattice spacing of 0.2 nm. Therefore, imaging a distorted lattice is challenging. Furthermore, interpreting TEM images with respect to a distorted lattice requires caution. A 2D projection of a distorted lattice may be an artifact produced by sample thickness and crystalline defects in a high-resolution TEM image[20,73], or by scan coil misalignment and image drift in a high-angle annular dark-field scanning transmission electron microscopy (HAADF-STEM) image.[90–92] To eliminate

such artifacts, several image correction and post-processing methods have been developed.[92–94] As the lattice strains are often measured or computed from TEM and STEM images with reference to an "unstrained" region,[16,84,95] the selection of the reference region is crucial in determining lattice strains. **Figure 5(a)** illustrates HADDF-STEM images of FeCoNiCrMn free from defects (e.g., dislocations),[24] which enables the calculation of lattice strain using the Geometric Phase Analysis (GPA) method (**Fig. 5(b)**).[67,96,97] Interestingly, the heterogeneous lattice strains found in FeCoNiCrMn demonstrates a fractal-like statistical characteristic[24], as seen in **Fig. 5(c)**. In addition to direct TEM imaging, Shao et al.[98] applied the scanning electron nanodiffraction (SEND) technique[99] to determine lattice distortion in HEAs. By carefully studying the distance change between diffraction beams, the authors finally obtained the strain mapping for FCC $Al_{0.1}CrFeCoNi$, as shown in **Figs. 5(d-e)**. Interestingly, the strain field determined by SEND is heterogenous and resembles a statistical fractal (**Fig. 5(f)**), which is similar to the results of GPA [**Figs 5(b-c)**].[98]

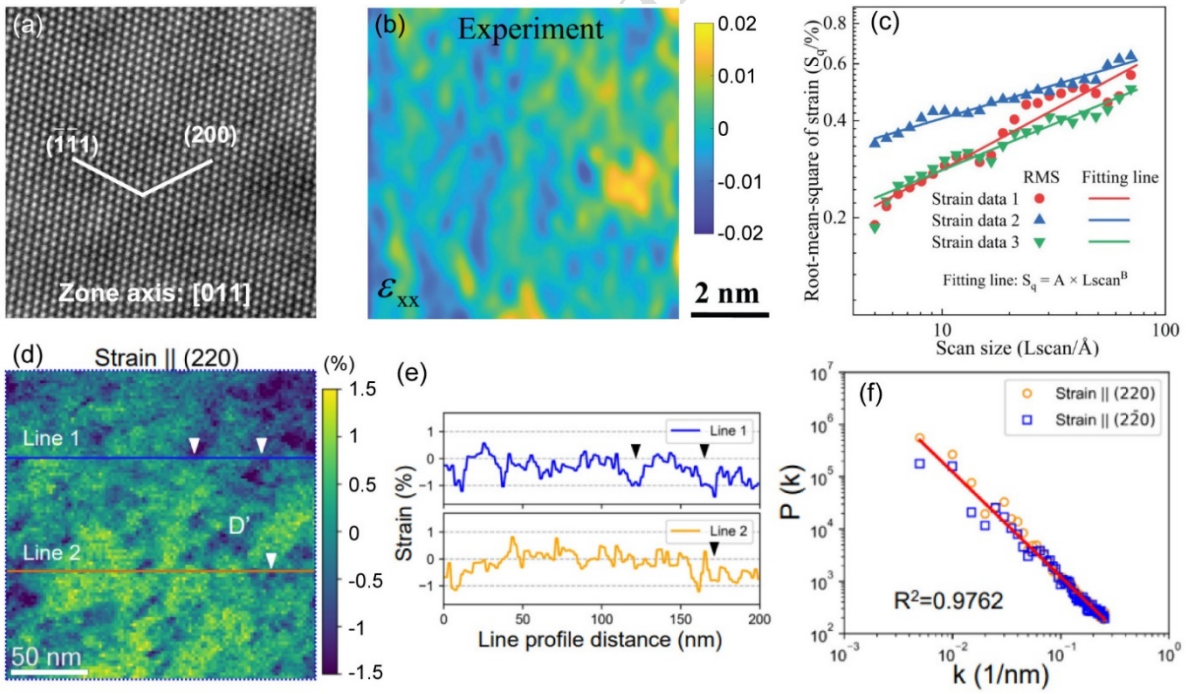

Figure 5. (a) The HAADF-STEM image with the [011] zone axis. (b) The strain mapping along the [111] direction. (c) The correlation between the RMS residual strain from the experiment and the scan size. Reproduced with permission.[24] (d) The strain mapping along the [220] direction. (e) The line profiles drawn from (d). (f) The correlation between intensity *P(k)* and

spatial frequency *k*. Reproduced with permission.[98]

Apart from the experimental methods, atomistic simulations, such as molecular dynamics simulations and first principles calculations, have been utilized to characterize lattice distortion in HEAs.[23,65,100–104] Notably, previous studies have commonly employed atomic bond length as a metric for lattice distortion.[23,65,100–103] For instance, Oh et al.[101] examined the local bond distortion in a special quasi-random structure (SQS) supercell of FeCoNiCrMn by analyzing the first nearest neighbor (1NN) bonds for the Mn atoms (**Figs. 6(a-b)**). The authors extracted the mean values of the distribution using Gaussian fits and compared them with results obtained from the extended X-ray absorption fine structure (EXAFS) (**Fig. 6(b)**), which showed good agreement.[101] Remarkably, the mean values of the atomic bond lengths were found to be one order of magnitude lower than the corresponding standard deviations. This behavior indicates that lattice distortion should be characterized by the magnitude of fluctuations in atomic bond length or angle, rather than by their volume-averaged value.[101] In other words, the averaged lattice strain in a distorted lattice is insignificant compared to the strain fluctuations, which is consistent with the geometric model developed by Ye et al.[23,53] Song et al.[103] also investigated the lattice distortion in BCC refractory HEAs and FCC 3d HEAs by comparing the 1NN-5NN atomic bond lengths, which revealed a much more pronounced distortion in the former.

Atomic displacement is another metric that can be used to quantify lattice distortion.[58,103,104] The total atomic displacement includes both dynamic and static components at finite temperature, but only the static component is linked to lattice distortion, as shown in **Fig. 6(c)**. Okamoto et al. [104] used synchrotron X-ray diffraction at 25 K to characterize the square of static atomic displacements in FeCoNiCrMn, which was found to be 23.5 pm^2 and matched the average value of mean-square atomic displacements (MSADs) obtained by first-principles calculations (**Fig. 6(d)**).[104] The MSADs of Cr and Mn were found to be larger than those of other elements, consistent with the strongest bond length variation for Cr and Mn in FeCoNiCrMn reported by Oh et al.[101] (**Fig. 6(d)**), indicating severe local

distortion around Cr and Mn atoms. Similarly, Song et al.[103] employed atomic displacement in their first-principles calculations to study lattice distortion, which showed an approximately positive linear relationship with the empirical atomic size mismatch parameter δ.[61]

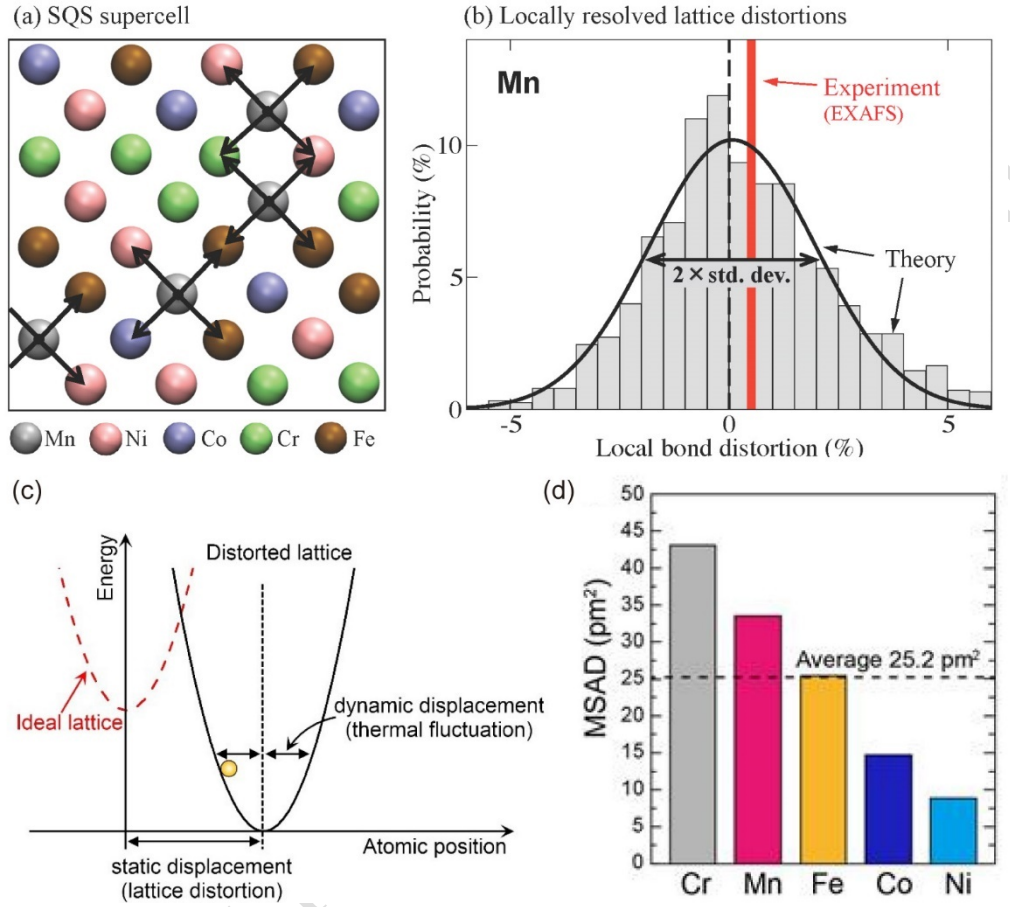

Figure 6. (a) Projection plot of an employed SQS model on the (110) plane. The black arrows mark the 1NN bonds for Mn atoms. (b) The distribution of local bond distortion. Reproduced with permission.[101] (c) Schematic illustration of an energy-position curve for a harmonic oscillator in the ideal and distorted lattice. (d) The calculated MSAD for various constituent atoms in FeCoNiCrMn. Reproduced with permission.[104]

As aforementioned, distorted lattices in HEAs exhibit both volumetric and shear strains.[22,53,105] To describe the heterogeneous strain field, Ye et al.[23] conducted extensive density function theory (DFT) calculations for CoCrFeNi and its sub-systems. Initially, the authors constructed a non-distorted lattice by relaxing the structure without altering the shape

of the face-centered cubic (FCC) unit cells (i.e., without shear strains).[23] They then lifted the prior restrictions on the shape of unit cells and performed further structure relaxation to calculate the heterogeneous strain field in the distorted lattice.[23] **Figure 7(a)** shows typical contour plots of local lattice strain components in CoCrFeNi, which fluctuate from atom to atom, similar to the experimental results shown in **Fig. 5**. However, the average volumetric and shear strains in the distorted alloys are both close to zero, as illustrated in **Fig. 7(b)**, indicating no net volume and shape change in the distorted alloys. These findings support the notion that lattice distortion should be characterized by strain fluctuations rather than average strains, which is consistent with the results reported in Ref.[101].

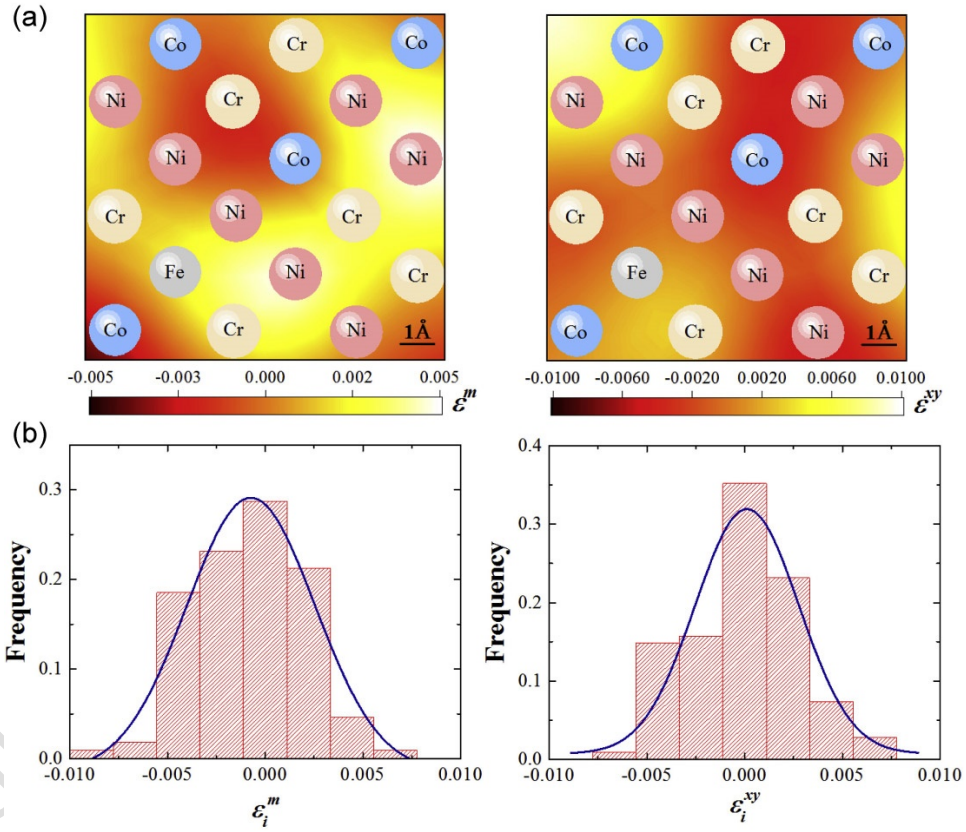

Figure 7. (a) The contour plots and (b) the distributions of the volumetric strain ε^m and shear strain ε^{xy}. Reproduced with permission.[23]

To sum up, characterizing lattice distortion, whether through experimental or computational means, involves quantifying the heterogeneous lattice strain field. The first

crucial step is to establish a reference lattice. In experimental techniques, such as TEM, the reference lattice can be determined by creating a "virtual" average lattice using the GPA method from a selected region,[96] or by identifying a unstrained region in nanobeam electron diffraction methods.[73] The accuracy of the determined lattice distortion relies on factors such as TEM spatial resolution, 2D projection nature, and sample thickness. On the other hand, total scattering methods provide the volume-average information about lattice distortion based on the PDF.[73] In atomistic simulations, like MD or DFT, the reference lattice can be constructed by assuming randomly packed atoms without static displacement from their ideal positions. This approach results in a reference lattice with a nearly identical lattice constant to the distorted lattice.[23] In other words, the average strains associated with lattice distortion can be neglected. Consequently, lattice distortion manifests as variation in the strain field,[23,53] which generally agrees with experimental findings.[53]

4. Mechanical Properties

4.1 Superelasticity and Elinvar Effect

According to the Ashby plot shown in **Fig. 8(a)**, conventional crystalline alloys typically have an elastic strain limit below 1% at room temperature due to the activation of crystalline defects such as dislocations[106]. In contrast, shape memory alloys (SMAs)[107], strain glass alloys[108–110] and Gum metals[111] can exhibit recovery strains of several percent. However, the superelasticity in these alloys originates from stress-induced phase transformation (e.g., martensitic phase transition), which often involves significant energy dissipation or mechanical hysteresis, constraining their use in applications that require high energy storage efficiency.[112–115] Recently, He et al.[28] developed an superelastic $(CoNi)_{50}(TiZrHf)_{50}$ HEA with an elastic limit of ~2% (**Fig. 8(a)**). Remarkably, this superelasticity arises from the large dislocation glide barriers that are enhanced by the severe lattice distortion, rather than any stress-induced phase transition before overall yielding. Consequently, this HEA exhibits a low loss factor and is free of mechanical hysteresis, which means that its energy storage efficiency is close to 100%. This

performance outperforms that of any superelastic materials previously reported.[116] Since atomistic simulations in Ref.[65,100] suggest that lattice distortion can reduce the elastic modulus while increase the yield strength, an improved elastic strain limit could possibly be achieved through increasing the degree of lattice distortion.[28,106] Moreover, it is worth pointing out that, unlike strain glass alloys,[117,118] lattice distortion induced superelasticity in HEAs is strain rate independent.[28]

In principle, decreasing structural defects with temperature increases elastic moduli, counteracting the decreasing moduli due to thermal expansion, resulting in temperature-independent elastic moduli (Elinvar effect) as seen in **Fig. 8(b)**[28]. Following this concept, Wang et al.[119] derived that the maximum temperature for the lattice distortion induced Elinvar effect (T_{El}) depends on the defect concentration (c) through the equation $T_{El} \propto \frac{\alpha\beta U_0}{C_v} c$, where α is a dimensionless constant (≈1); β is a parameter directly related to the anharmonicity of an interatomic potential (≈40 for crystals[120]); U_0 is the cohesive energy and C_v is the constant specific heat. Accordingly, such non-magnetic originated Elinvar effect should be favorable when the defect is adequate and can be tuned by temperature. For HEAs, lattice distortion is associated with a lattice strain or an effective molar fraction of lattice defects of ~10^{-2}[53,121] and can be easily tailored through lattice expansion at high temperatures[28], making HEAs a good candidate Elinvar alloy. Further studies demonstrated that a reduced lattice distortion, which is revealed through alloying Fe into the Elinvar alloy $(CoNi)_{50}(TiZrHf)_{50}$, indeed induces a decline in the Elinvar effect (**Fig. 8(b)**). In addition, the temperature range of the lattice distortion-induced Elinvar effect is wider than that for the Gum metal ($Ti_{73.2}Nb_{23}Ta_{0.7}Zr_2O_{1.2}$), [111] $Fe_{63.4}Mn_{30.62}Si_{5.31}C_{0.67}$,[37] and the strain glass alloys (i.e., $Ti_{49.2}Ni_{50.8}$[122] and $Mn_{60}Cu_{40}$[123]), as shown in **Fig. 8(c)**.

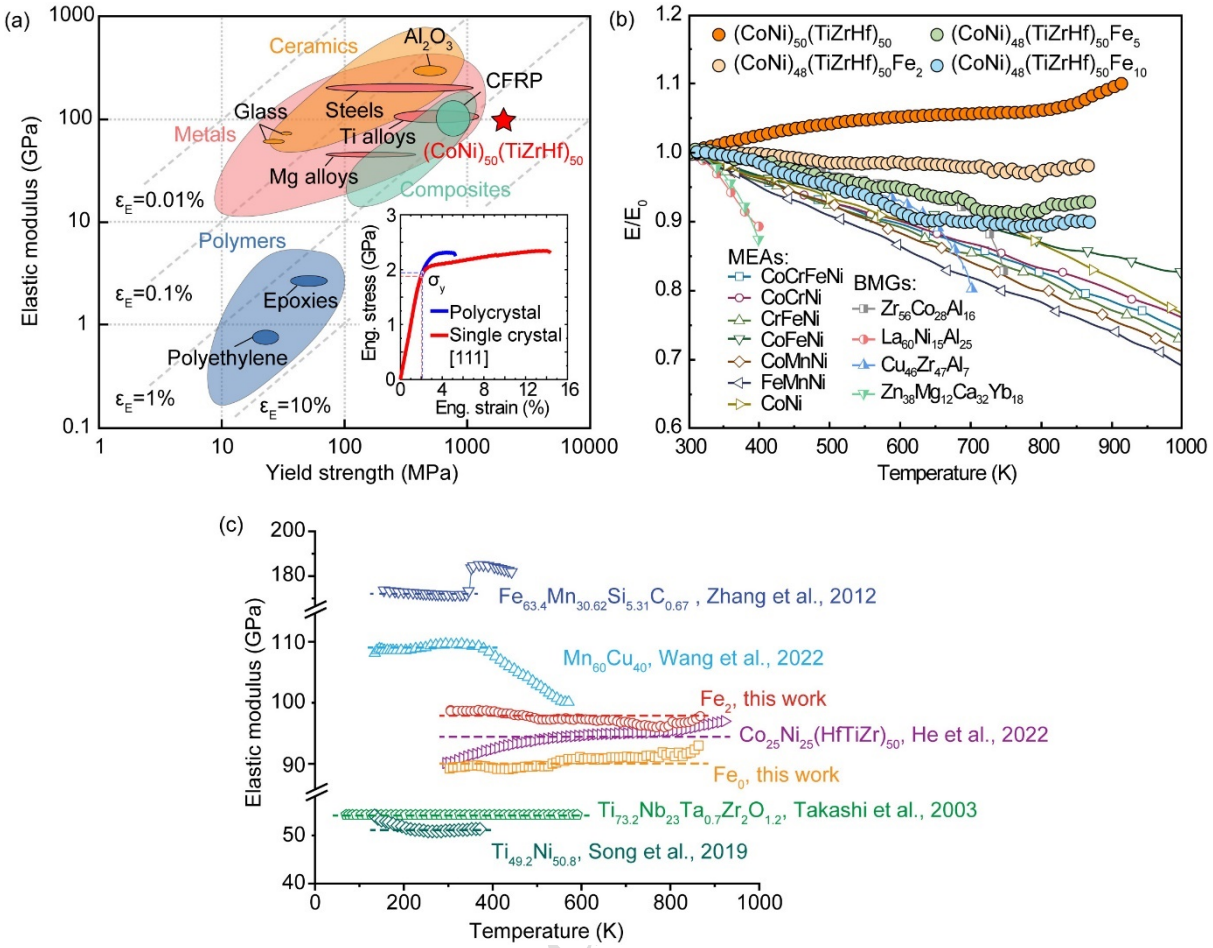

Figure 8. (a) Ashby plot of elastic modulus versus yield strength[124]. The inset shows the stress-strain curves of $(CoNi)_{50}(TiZrHf)_{50}$. (b) Young's modulus versus temperature of the $(CoNi)_{50-x}(TiZrHf)_{50}Fe_x$ (x=0, 2, 5 and 10) alloys compared with other metallic materials, such as medium-entropy alloys (MEAs) and bulk metallic glasses (BMGs). E_0 = Young's modulus at room temperature. (c) Elastic modulus versus temperature of the distorted HEAs compared with other Elinvar alloys. Reproduced with permission.[28,119]

4.2 Strength-Plasticity Synergy

The interaction between lattice defects and microstructure is the underlying mechanism for the plastic properties of crystalline solids, and the behavior of lattice defects can be understood thermodynamically from the energy barriers for defect activation and the free energy changes caused by defect motion.[125] Mean-field approaches were used to fully study these mechanisms for conventional alloys, as discussed in **Section 2**. However, due to the heterogeneous strain

field in HEAs,[24,98] mean-field theories are no longer appropriate. To investigate plasticity in FeCoNiCrMn, Li et al. [24] developed a three-dimensional discrete dislocation dynamics (DDD) simulation approach by incorporating the heterogeneous strain field obtained from experiments (**Fig. 5(b)**) into DDD simulations. **Figure 9(a)** shows the initial dislocations embedded in the simulation cells. In the presence of the heterogeneous strain field, dislocations can multiply and be activated in multiple slip systems through the enhanced Frank-Read source mechanism, leading to extensive dislocation forest strengthening. Furthermore, dislocations become wavy as they traverse the heterogeneous strain field, as shown in **Fig. 9(b)**. Their movement is slowed down in regions of compressive stresses and accelerated in regions of tensile stresses, leading to an apparent local pinning effect that makes overall dislocation movement sluggish, increases dislocation densities, and improves the strength of the distorted alloy. The heterogeneous strain field also favors double cross-slips (**Fig. 9(c)**) as well as the formation of multiple jogs (**Fig. 9(d)**), improving the overall plasticity of the distorted alloy. However, all these effects related to the strength-plasticity synergy disappear in the absence of the heterogeneous strain field.[24]

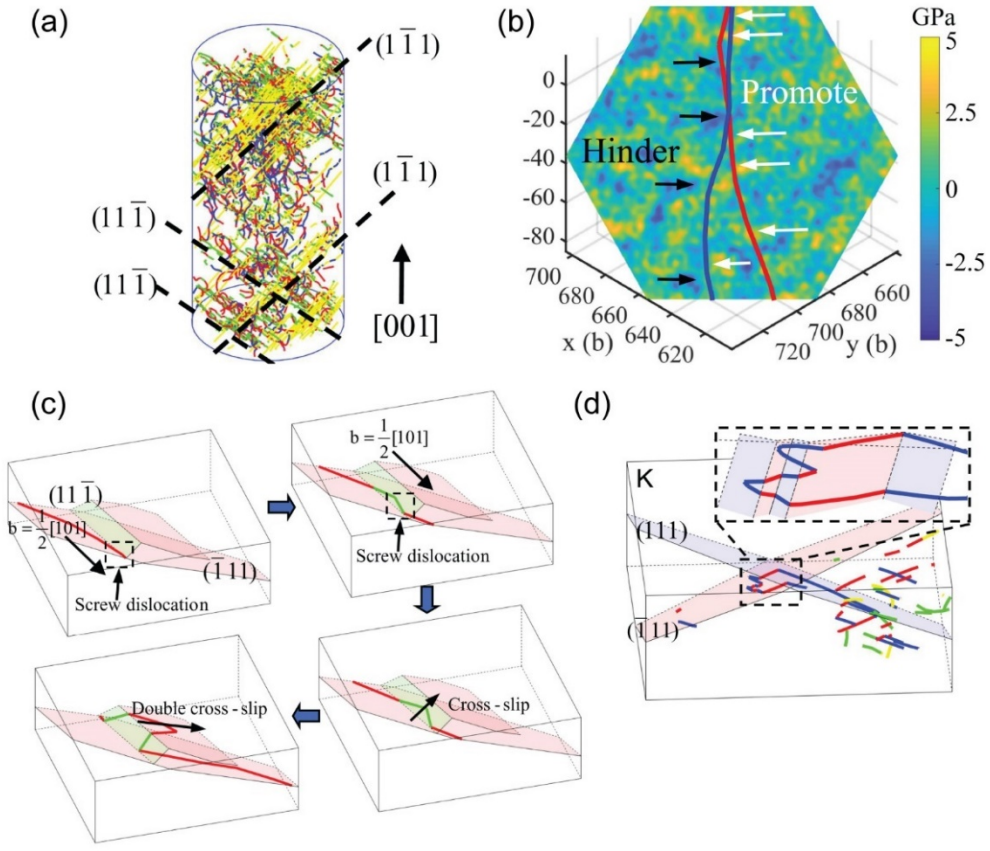

Figure 9. (a) The dislocation configuration in the micropillar at strain of 0.57%. (b) The dislocation configuration of the Frank-Read source under the heterogeneous strain field. The red and blue lines indicate FR sources with source lengths of 1,500 and 2,000 *b*, *b* is the magnitude of the Burgers vector. (c) The process of cross slip and double cross slip. (d) Many jogs appear on a dislocation benefiting from the multiple double cross slips. Reproduced with permission.[24]

The lattice distortion-induced strengthening in HEAs has been theoretically modeled from the perspective of solid solution strengthening.[51,59,60,126–130] To extend the original Labusch model[50] to concentrated multicomponent solid solutions, Toda-Caraballo et al. accounted for solute-solute interactions and embedded lattice distortion in an interatomic spacing matrix[131]. Varvenne et al.[59,60] also proposed a theory for random FCC HEAs, in which the interaction of dislocations with misfit volumes of solutes results in the strengthening effect. The random distribution of solutes induces local energy fluctuations, converting an initially straight dislocation line into a wavy configuration in order to minimize the total energy of the entire alloy system, which is consistent with the observations in the DDD simulations[24] (**Fig. 9**). For BCC HEAs, Rao et al.[128] extended the Suzuki model[132,133] to predict their strengths, in which the dominant strengthening mechanism is the impedance of kink glide by solutes. In comparison, Maresca et al.[129] proposed a strengthening theory in the framework developed by Varvenne et al.,[59,60] which considers strengthening by jog formation as evidenced in experiments at high temperatures. Unlike the traditional perspective of screw dominance in BCC alloys,[13] Maresca et al.[130] proposed that the strength in BCC HEAs can be controlled by edge dislocations due to the large energy barriers created by random solute environments.

In addition to simulations and theories, increasing experiments have verified the positive effect of lattice distortion on the strength-plasticity synergy witnessed in HEAs. Sohn et al.[29] found severe lattice distortion in VCoNi, which manifests as the largest value of mean square atom displacement ($MSAD^{1/2}$) compared to a variety of FCC HEAs (**Fig. 10(a)**). With

increasing strain in the distorted lattice, planar dislocation glide was predominant at the early stage of plasticity (**Fig. 10(b)**), followed by the formation of dense dislocation networks possibly due to cross slips (**Figs. 10(c-d)**), which impedes mobile dislocations, thereby enhancing the dislocation storage ability for strain hardening. As a result, this distorted alloy exhibits both high yield strength (~1 GPa) and ductility (~38%). Wang et al.[25] found that the moving dislocation would increase lattice distortion in the slip channels (**Figs. 11(a-b)**) in BCC $Ti_{50}Zr_{18}Nb_{15}V_{12}Al_5$ HEA by destroying local chemical order, resulting in dislocation pile-ups and the activation of secondary slip channels as seen in **Figs. 11(c-d)**. As a result, this alloy exhibited a yield strength of 980 MPa and fracture strain of 24.7% under tension at room temperature.

Lattice distortion also has a significant influence on the mechanical properties at elevated temperatures. Lee et al.[121,134] studied the effect of lattice distortion on the mechanical performance of BCC NbTaTiV HEA at both room and elevated temperatures. Through heat treatments, the initial compositional segregation was eliminated, and the lattice distortion effect was maximized, resulting in a compressive yield strength of 1273 MPa and a final strain greater than ~30% at room temperature. After increasing the temperature to 900 ℃, the strong hardening capability could still be retained with a yield stress of 688 MPa, which was attributed to the relatively slow diffusion and strong softening resistance induced by lattice distortion at the elevated temperature.

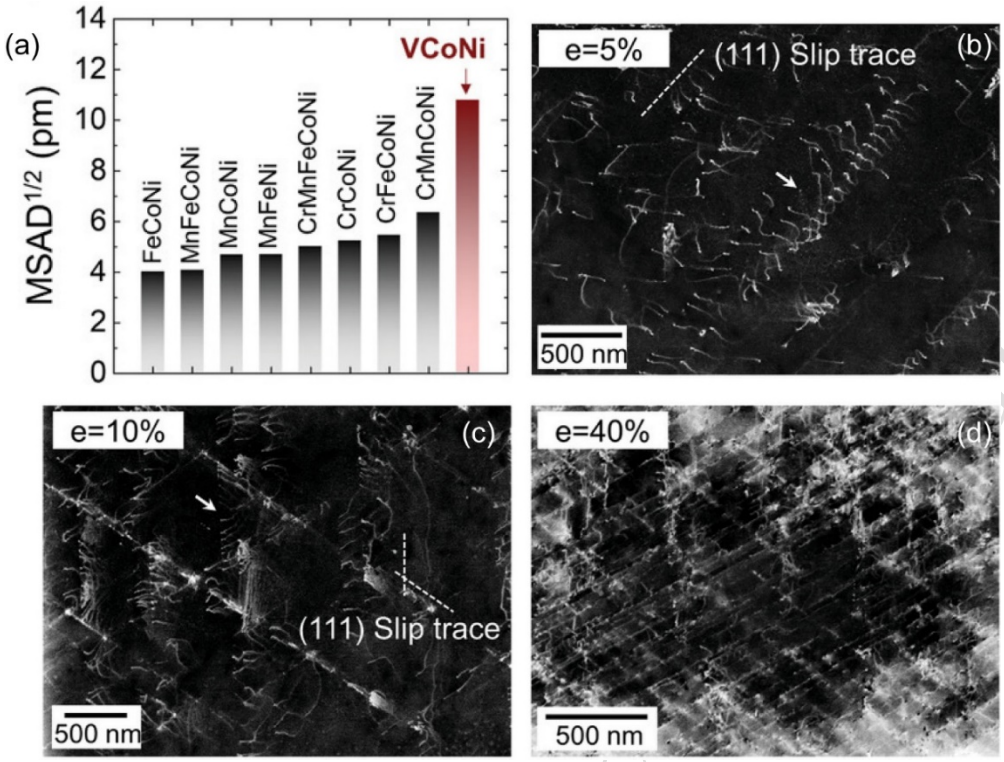

Figure 10. (a) MSADs for various MPEAs. The electron channeling contrast images for (b) 5%, (c) 10% and (d) 40% deformed CoNiV alloys revealing the formation of nanosized planer dislocation substructures. Reproduced with permission.[29]

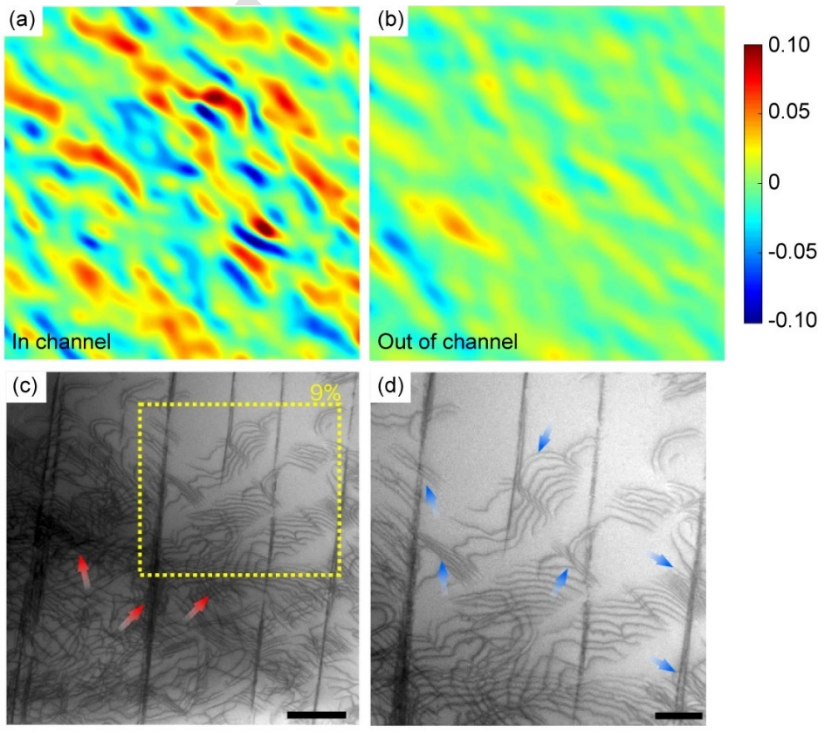

Figure 11. The atomic elastic strain mappings of two regions (a) in and (b) out of a slip channel. (c) The STEM images of $Ti_{50}Zr_{18}Nb_{15}V_{12}Al_5$ at strain of 9%. (d) The enlarged image of the yellow-dot-boxed area in (c). Red arrows mark the dislocation tangles at the intersections of second-generation channels. Blue arrows mark the dislocation pile-ups against the first-generation channels. Reproduced with permission.[25]

5. Transport Properties

5.1 Sluggish versus Fast Atom Diffusion

HEAs, like conventional alloys, utilize point defects, such as interstitial atoms and vacancies, for atom diffusion, and the properties of these defects, including their formation and migration energies, govern the diffusion behavior of atoms in HEAs. While lattice distortion can influence the energy landscape of these defects, there is still some debate over its specific role in atom diffusion.[135] Previous research by Tsai et al.[136] demonstrated that the FCC $CoCrFeMn_{0.5}Ni$ HEA had a lower diffusion coefficient than its constituent elements and Fe-Cr-Ni alloys, and the corresponding activation energies, normalized by the alloy's melting temperature, were higher. These elevated energy barriers for vacancy migration were attributed to the mixing enthalpies arising from the combination of multiple principal elements, which were implicitly influenced by lattice distortion. Zhao et al.[137] conducted a more detailed study and found that the BCC VTaCrW HEA had a wider range of vacancy formation energies than FCC HEAs due to its larger atomic volume misfit. The formation energy of vacancies that substitute V and Cr decreased in the distorted lattice compared with that in pure metals, while there were higher fluctuations in the formation energy of vacancies that substitute Ta and W. These results revealed a complex diffusion behavior of atoms in a severely distorted lattice.

Recent research has yielded conflicting findings on the role of lattice distortion in the diffusion behavior of HEAs. For example, Zhao et al.[138] reported that larger lattice distortion, as evidenced by the interatomic distance variation in BCC TiVTa, led to lower interstitial formation energy, diffusivity, and higher interstitial diffusion activation energy than in BCC

TiVTaNb, supporting the idea that lattice distortion contributes to sluggish diffusion. However, other studies have shown that lattice distortion can accelerate constituent diffusion in different HEAs. For instance, the mean migration energy of Ta in BCC VTaCrW was even lower than in pure Ta;[137] and faster diffusion of Zr was observed in BCC TiZrHfNbTa and TiZrHfNbV HEAs compared to the geometric mean of their constituents. This phenomenon was attributed to a lattice mismatch δ greater than 3%.[139] In addition, the diffusion coefficients and activation energies of Ti in HCP HEAs, such as HfTiZr, $Al_5Hf_{25}Sc_{20}Ti_{25}Zr_{25}$, and $Al_{15}Hf_{25}Sc_{10}Ti_{25}Zr_{25}$, were found to be lower than in α-Ti. The higher δ and mean squared atomic displacements (MSAD) in $Al_5Hf_{25}Sc_{20}Ti_{25}Zr_{25}$ and $Al_{15}Hf_{25}Sc_{10}Ti_{25}Zr_{25}$ than in HfTiZr and FCC or BCC HEAs promoted the diffusion of Ti.[140] Despite the ongoing controversy, sluggish diffusion in specific HEAs cannot be ruled out and warrants further research.

5.2 Ultralow Lattice Thermal Conductivity

Thermal conductivity in metals is contributed by both electrons and phonons, with the total thermal conductivity given by $\kappa = \kappa_e + \kappa_{ph}$. HEAs have a significantly larger lattice thermal conductivity κ_{ph} compared to their electronic thermal conductivity κ_e, as reported by Jin and Bei.[141] Previous intensive studies[142–144] have found that lattice distortion in an alloy greatly influences its lattice thermal conductivity. Abeles developed a point defect theory in the 1960s and attributed low κ_{ph} in chemically disordered alloys to phonon scattering caused by atomic mass and lattice strain fluctuations.[145] In certain HEAs, such as the Zr-Hf-Ni-Pd-Sn-Sb system,[146] lattice strain-induced scattering is much larger than that of mass fluctuation-induced scattering. The ultralow lattice thermal conductivity in HEAs can lead to exceptional thermoelectric performance, which can be evaluated by the figure of merit $zT = S^2\sigma T/(\kappa_e + \kappa_{ph})$,[142,144] where S, σ and T denote the Seebeck coefficient, electrical conductivity and absolute temperature, respectively. The figure of merit can be maximized by decreasing the thermal conductivity while maintaining the electrical conductivity, provided that other parameters remain unchanged.

Hu et al.[147] reported a ultralow lattice thermal conductivity of ~ 0.32 W/(m·K) at 900 K in a SeTe based chemically complex alloy. Due to lattice distortion, this alloy achieved a high figure of merit $zT \approx 1.42$. Recently, Jiang et al.[32,148,149] designed several high-performance HEA thermoelectrics based on the strategy of lattice distortion. By tuning electron and phonon localization, they achieved a record-breaking figure of merit value $zT \approx 2.7$ at 750 K.[149] First-principles calculations revealed that the shear strain components in a lattice distortion induced strain field are significantly larger than the normal strain components, being consistent with experimental measurements[32] and recent theories.[23] This contrasts with the early theoretical model of Varvenne et al.,[59] which only considered normal strains in the lattice distortion effect. **Figure 12** shows the temperature-dependent thermal conductivity of various metals and alloys with distinct atomic size misfit. Less distorted metals or alloys, with $\delta < 0.3\%$, show higher thermal conductivities than distorted alloys with $\delta > 0.3\%$. Moreover, the thermal conductivities of the former kind of metals decrease with increasing temperature, which can be attributed to anharmonic scattering caused by excessive atom vibrations (e.g., the dynamic component of lattice distortion).[150] Conversely, the thermal conductivities of the latter alloys increase with increasing temperature, possibly due to the lessening of lattice distortion caused by atomic size misfit (e.g., the static component of lattice distortion) at high temperatures, as discussed in He et al.[28] and Wang et al.[119]

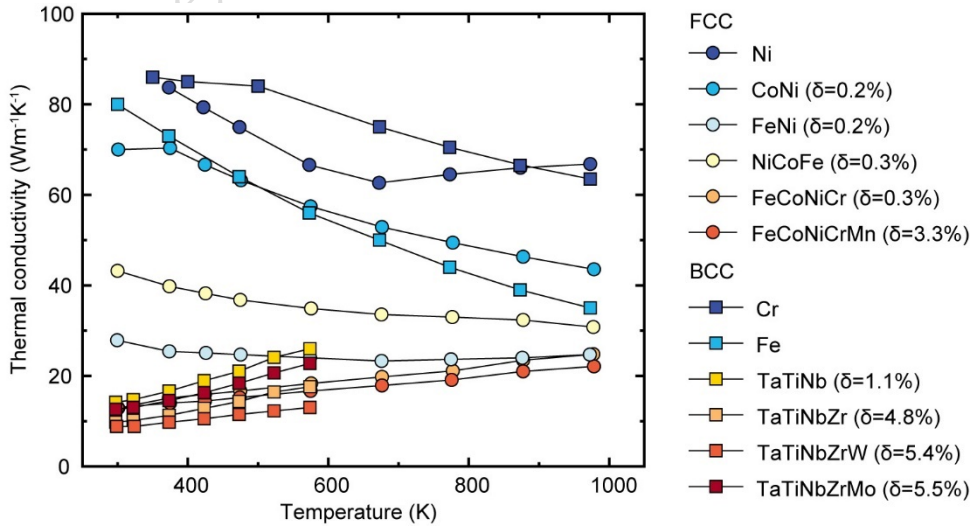

Figure 12. Thermal conductivity of FCC and BCC HEAs, compared with that of conventional

FCC alloys (Ni, CoNi and FeNi) and BCC alloys (Cr and Fe). δ is the empirical parameter of atomic size misfit (see in **Section 2**).[61] Data come from Refs.[141,151,152]

6. Irradiation Resistance

In general, irradiation damage can manifest as hardening, embrittlement and swelling at the macroscale, as well as phase instability and elemental segregation at the microscale.[141,153] These phenomena stem from the formation, migration and evolution of defects under the synergy effect of irradiation conditions and intrinsic microstructure. Thus, mechanistic research on radiation resistant HEAs has focused on the tailoring of defect behavior. According to Ref.[33,141,153], reducing thermal conductivity can retard energy dissipation during collision cascade and facilitate recombination for vacancies and interstitial atoms, which explains the lower extent of radiation damage produced in FeCoNiCr than that in conventional alloys (e.g., Ni and CoNi).[33,141,153] The defect recombination process can also be understood from the migration energies of defects, which are a single value in conventional alloys,[141,153,154] and have a distribution in HEAs due to the distortion effect.[26,141,153,154] Consequently, the overlap between the migration energies for interstitials and vacancies produce strong interactions between point defects and enhance their recombination, as reported in FeCoNiCr.[154]

In contrast to the one-dimensional (1D) motion of small interstitial clusters in conventional alloys (**Fig. 13(a)**),[34,155,156] Lu et al.[34] found that the migration mode of interstitial clusters in alloys with large atomic size misfit is three dimensional (3D), as evidenced by molecular dynamics (MD) simulations (**Fig. 13(c)**). As a result, most of the interstitial clusters remain in the defect production region, facilitating recombination with vacancies and/or trapping by other defects such as dislocation loops (**Fig. 13(d)**), instead of agglomerating in deep regions and leaving a detrimental high-vacancy supersaturation in the shallow region (**Fig. 13(b)**).[34] Recently, Chen et al.[157] applied DDD simulations to investigate the irradiation hardening behavior of FeCoNiCr. They found that the heterogeneous strain field leads to extensive cross-slips, suppressing the irradiation-induced hardening via enhancing the capability of plastic

deformation.[157]

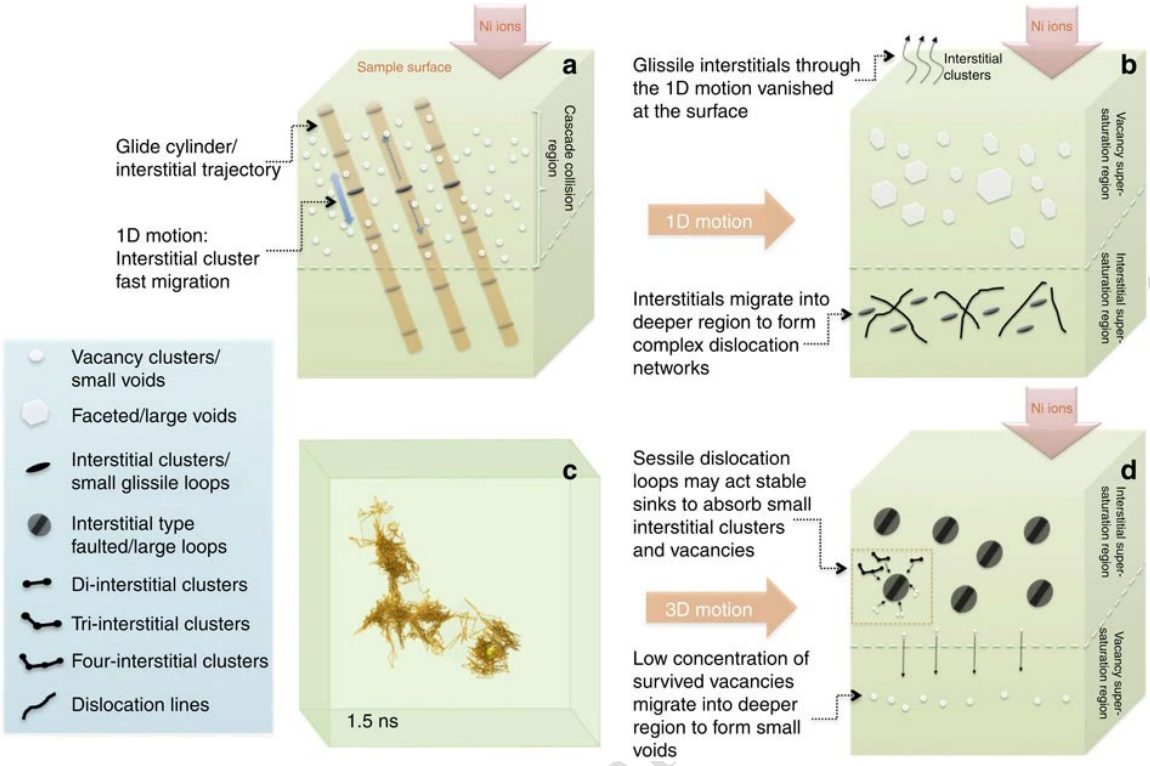

Figure 13. Schematic plot of (a) 1D motion and (b) defect evolution and distribution as a result of (a). (c) MD simulation result of the trajectory of the center of a four-interstitial cluster showing a 3D migration mode. (d) Schematic plot of defect evolution and distribution as a result of (c). Reproduced with permission.[34]

Increasing efforts have been devoted to studying various HEAs as potential irradiation-resistant materials for applications in nuclear industries.[33,34,39,158–162] The cross-sectional TEM images of the damaged region in FCC FeCoNiCrMn and Ni irradiated by Ni ions at 773 K are shown in **Fig. 14(a)**.[34] The evidently fewer and smaller voids in FeCoNiCrMn indicate better swelling-resistance, as exemplified by **Fig. 14(b)**.[39] Similarly, Su et al.[158] found excellent swelling-resistance in single-phase BCC AlCrFeV irradiated by Au ions at 773 K, and attributed it to the large atomic size misfit. Moreover, micro-and nano-scale mechanical tests (e.g., micropillar tests and nanoindentation) revealed that some BCC HEAs, including AlCrFeV,[158] MoNbTaTiW,[159] HfTaTiVZr,[160] $Ti_2ZrHfV_{0.5}Mo_{0.2}$[161] and $W_{38}Ta_{36}Cr_{15}V_{11}$[162]

show extremely weak irradiation-induced hardening, compared to that observed in Fe[158] and stainless steel[160] under the same irradiation conditions.

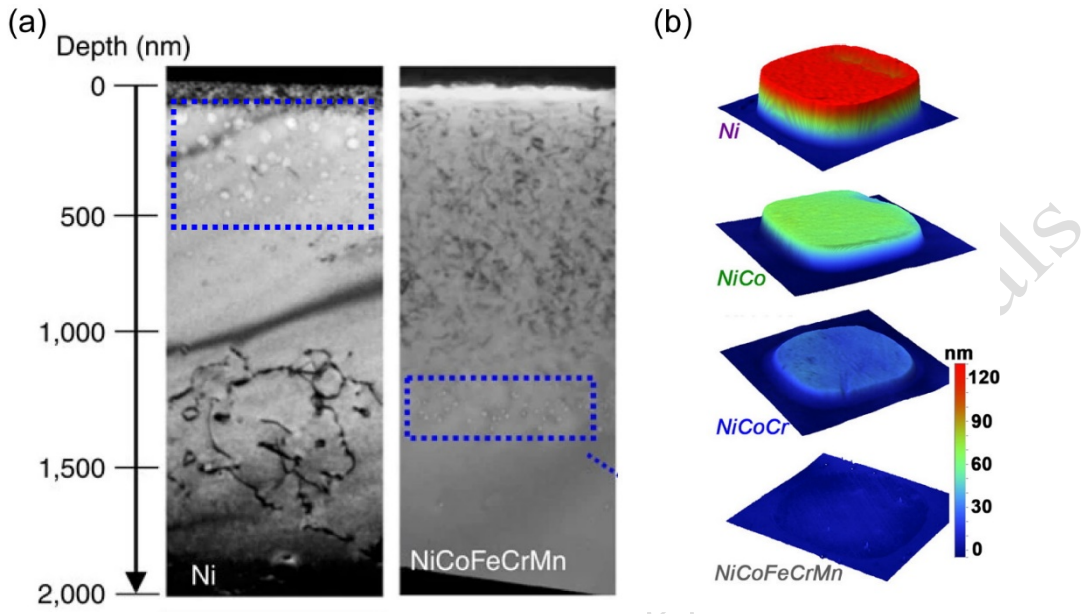

Figure 14. (a) Cross-sectional TEM images of Ni and NiCoFeCrMn after irradiation. The blue boxes highlight the voids regions. Reproduced with permission.[34] (b) Surface step measurements of Ni, NiCo, NiCoCr, and NiCoFeCrMn after irradiations. Reproduced with permission.[39]

7. Electrochemical Catalytic Properties

Elastic strains have been shown to play a significant role in catalytic reactions.[163–165] Therefore, heterogeneous strain fields found in distorted HEAs make them a promising candidate for electrocatalytic materials.[166] The adsorption free energy of alloys can be tuned by elastic strains, which can reduce the energy barrier against catalytic reactions (**Fig. 15(a)**).[167] Additionally, lattice strains can lower the formation energy of defects, which can lead to the creation of abundant defects such as oxygen vacancies.[166] The center of electron d-band can also be regulated by lattice strains,[165] which is known to scale with the adsorption energy of reactants and intermediates. Typically, an upshift of the d-band center results in a stronger metal-molecule interaction, while a downshift leads to weaker binding, as depicted in **Fig. 15(b)**.[163] Due to lattice distortion-induced heterogeneous elastic strains, many researchers

have focused on developing HEA-based catalysts for various electrochemical reactions, such as the hydrogen evolution reaction (HER), oxygen evolution reaction (OER), oxygen reduction reaction (ORR), methanol oxidation reaction (MOR), and CO_2 reduction reaction (CO_2RR).[168–174] While Pt/Pd-based catalysts show excellent performance in HER due to proper binding energy, their high cost makes mass production challenging. However, doping Pt/Pd into HEAs not only greatly reduces costs, but also introduces severe lattice distortion with strain (**Fig. 15(c)**)[174] and tunes the electronic structure, resulting in excellent performance and stability.[168] Similarly, Ru and Ir can be doped with non-noble metals to form distorted HEAs, resulting in various successful HEA catalysts for OER.[168–170] For ORR, Pt-containing catalysts are also preferred, and the IrPdPtRhRu HEA exhibits a low overpotential and outperforms commercial Pt/C.[171] The catalytic activity of BCC AlCoCrTiZn HEA powder for azo-dye degradation was reported to be excellent, which was explained by the lattice distortion-induced strains.[172] The $Pt_{50}Fe_{11}Co_{10}Ni_{11}Cu_{10}Ag_8$ film was shown to be a highly active and stable catalyst toward MOR, while HEA nanoparticles AuAgPtPdCu demonstrated enhanced selectivity for CO_2RR.[173] Moreover, it has been discovered that lattice strains in multiphase HEAs can guide dealloying, enabling selective etching of certain elements or phases to create a larger surface area.[164,175–179] The resulting structure from dealloying can also aid in adjusting surface lattice strains.[164]

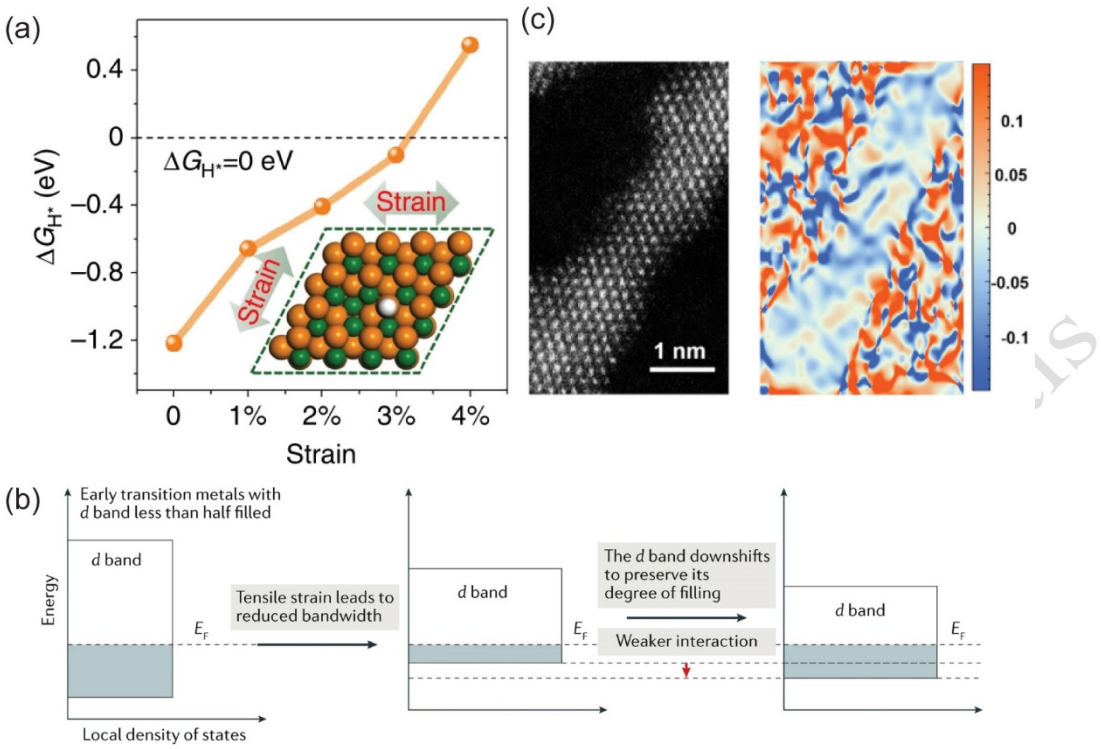

Figure 15. (a) Hydrogen adsorption free energy (ΔG_{H^*}) versus tensile strain for the CoO {111}-Ov surface. The surface O-vacancy concentration on {111}-Ov is ~11.1%. Reproduced with permission.[167] (b) Energy diagrams showing the effect of tensile strain on the d-band position of late transition metals. Reproduced with permission.[163] (c) The HAADF-STEM image and corresponding strain map of Pt/Pd-containing HEA. Reproduced with permission.[174]

8. Data Driven Design of Distorted Alloys

In order to create effective distorted HEAs, it is important to maximize the atomic size difference between constituent elements while maintaining their random distribution within a common lattice. However, it is worth noting that when the atomic size difference exceeds a certain threshold, such as 6.5%, a single-phase lattice structure can undergo a transition to a multi-phase structure, potentially leading to the formation of precipitates.[11,61,180–182] Moreover, as the atomic size difference continues to increase, surpassing a critical value (δ>8%), a distorted lattice can collapse and transform into a metallic glass. Therefore, the challenge in designing a distorted HEA lies in increasing the atomic size difference while maintaining the

stability or metastability of its crystalline structure with a high degree of chemical randomness.

In recent years, data-driven approaches, such as machine learning and statistical methods, have shown promise in accelerating the design of distorted HEAs. For example, Zhou et al. [183] utilized a supervised machine learning model to study the synergistic effect of thirteen different design parameters on phase selection in HEAs. They found that the atomic size difference parameter δ plays a significant role in the formation of a solid solution phase. Specifically, to form a solid solution, the atomic size difference must be minimized, while the formation of amorphous and intermetallic phases is not sensitive to δ. Huang et al.[184] also employed machine learning models to predict lattice distortion and phase stability in the Co-Ni-Cr-Mo-V HEA system, as depicted in **Fig. 16**. Interestingly, their results revealed that the electronegativity difference was more important than atomic size misfit in determining the lattice distortion as quantified by the mean square atomic displacement (MSAD)[184] in the Co-Ni-Cr-Mo-V system, which merits further investigations. Additionally, Tandoc et al.[185] developed a physics-informed statistical model to predict lattice distortion for refractory HEAs. This model established a linear relationship between root mean square atomic displacement (RMSAD), as the measure of lattice distortion, and the physical properties of interatomic bonding. The authors[185] also proposed a simple expression based on RMSAD to predict the room-temperature yield strength of refractory HEAs. These studies demonstrate the potential of data-driven approaches to accelerate the design of distorted HEAs with desirable properties.

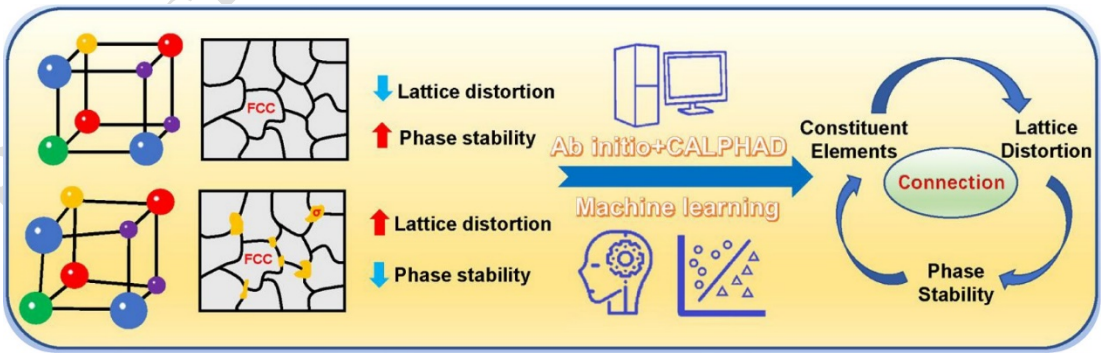

Figure 16. Graphic illustration of the machine learning model. Reproduced with permission.[184]

9. Summary

To sum up, HEAs have been the focus of extensive research since their introduction in 2004.[9,10] These materials possess a complex chemical composition resulting in a unique crystalline structure characterized by lattice distortion. This structural feature has a profound impact on various physical and mechanical properties of HEAs, including elasticity, yield strength, strain hardening mechanisms, diffusion dynamics, thermal conductivity, irradiation resistance, and catalytic performance. In traditional alloys, lattice distortion is primarily caused by solute atoms, resulting in a well-defined elastic strain field consistent with Eshelby theory.[52] However, in HEAs, the lattice distortion exhibits a highly fluctuating elastic strain field that can vary significantly from one atom to another, making it challenging to use classical models to develop structure-property correlations. To address this challenge, people have employed various atomistic simulations and state-of-the-art experimental approaches to characterize lattice distortion in HEAs and understand how it affects the movements of crystalline defects, such as dislocations, from the perspective of a rugged potential energy landscape.[24,60,126] These studies have shown that the severe lattice distortion in HEAs could lead to unique multifunctional properties that are unprecedented in conventional alloys.

However, excessive lattice distortion can lead to lattice destabilization, resulting in phase transition and even amorphization. Moreover, lattice distortion can also be coupled with chemical ordering or CSRO.[64–68] In certain HEAs, such as the Elinvar alloys Co-Ni-Ti-Zr-Hf-Fe, the formation of CSRO, as highlighted in Ref.[119], may reduce lattice distortion, which is detrimental to superelasticity of the HEAs. Therefore, it is essential to comprehend the interplay between lattice distortion and CSRO to advance the development of multifunctional HEAs. In our perspective, the key to designing multifunctional HEAs through lattice distortion lies in maximizing atomic size misfit while simultaneously ensuring the stability of the distorted lattice. However, these two objectives often conflict, resulting in a trade-off during the design of lattice distortion-enabled multifunctional HEAs.

Acknowledgements

YY acknowledges the financial support provided by the Research Grants Council, the Hong Kong Government, through the General Research Fund with the grant numbers (CityU 11201721, CityU11200719 and CityU11213118).

References

[1] W. D. Callister, D. G. Rethwisch, *Materials Science and Engineering: An Introduction*, John Wiley & Sons, New York, **2007**.

[2] Q. F. He, Z. Y. Ding, Y. F. Ye, Y. Yang, *JOM* **2017**, *69*, 2092.

[3] M. C. Gao, J.-W. Yeh, P. K. Liaw, Y. Zhang, *High-Entropy Alloys: Fundamentals and Applications*, Springer, **2016**.

[4] J. W. Yeh, Y. L. Chen, S. J. Lin, S. K. Chen, in *Mater. Sci. Forum*, Trans Tech Publ, **2007**, pp. 1–9.

[5] J. R. Davis, *Copper and Copper Alloys*, ASM International, **2001**.

[6] M. Ghasri-Khouzani, J. R. McDermid, *Mater. Sci. Eng. A* **2015**, *621*, 118.

[7] X. Yuan, Y. Zhao, X. Li, L. Chen, *J. Mater. Sci. Technol.* **2017**, *33*, 1555.

[8] R. E. Smallman, A. H. W. Ngan, in *Phys. Metall. Adv. Mater. Eng.*, Butterworth-Heinemann, Oxford, **2007**, pp. 447–480.

[9] J. W. Yeh, S. K. Chen, S. J. Lin, J. Y. Gan, T. S. Chin, T. T. Shun, C. H. Tsau, S. Y. Chang, *Adv. Eng. Mater.* **2004**, *6*, 299.

[10] B. Cantor, I. T. H. Chang, P. Knight, A. J. B. Vincent, *Mater. Sci. Eng. A* **2004**, *375–377*, 213.

[11] Y. F. Ye, Q. Wang, J. Lu, C. T. Liu, Y. Yang, *Mater. Today* **2016**, *19*, 349.

[12] E. P. George, D. Raabe, R. O. Ritchie, *Nat. Rev. Mater.* **2019**, *4*, 515.

[13] E. P. George, W. A. Curtin, C. C. Tasan, *Acta Mater.* **2020**, *188*, 435.

[14] W. Li, D. Xie, D. Li, Y. Zhang, Y. Gao, P. K. Liaw, *Prog. Mater. Sci.* **2021**, *118*, 100777.

[15] J. W. Yeh, *Ann. Chim. Sci. des Mater.* **2006**, *31*, 633.

[16] J. W. Yeh, *JOM* **2015**, *67*, 2254.

[17] M.-H. Tsai, J.-W. Yeh, *Mater. Res. Lett.* **2014**, *2*, 107.

[18] J.-W. Yeh, *JOM* **2013**, *65*, 1759.

[19] Z. P. Lu, H. Wang, M. W. Chen, I. Baker, J. W. Yeh, C. T. Liu, T. G. Nieh, *Intermetallics* **2015**, *66*, 67.

[20] E. J. Pickering, N. G. Jones, *Int. Mater. Rev.* **2016**, *61*, 183.

[21] R. K. Nutor, Q. Cao, X. Wang, D. Zhang, Y. Fang, Y. Zhang, J.-Z. Jiang, *Adv. Eng. Mater.* **2020**, *22*, 2000466.

[22] Q. He, Y. Yang, *Front. Mater.* **2018**, *5*, 42.

[23] Y. F. Ye, Y. H. Zhang, Q. F. He, Y. Zhuang, S. Wang, S. Q. Shi, A. Hu, J. Fan, Y. Yang, *Acta Mater.* **2018**, *150*, 182.

[24] J. Li, Y. Chen, Q. He, X. Xu, H. Wang, C. Jiang, B. Liu, Q. Fang, Y. Liu, Y. Yang, P. K. Liaw, C. T. Liu, *Proc. Natl. Acad. Sci. U. S. A.* **2022**, *119*, e2200607119.

[25] L. Wang, J. Ding, S. Chen, K. Jin, Q. Zhang, J. Cui, B. Wang, B. Chen, T. Li, Y. Ren, S. Zheng, K. Ming, W. Lu, J. Hou, G. Sha, J. Liang, L. Wang, Y. Xue, E. Ma, *Nat. Mater.* **2023**, 1.

[26] Y. Zeng, B. Ouyang, J. Liu, Y. W. Byeon, Z. Cai, L. J. Miara, Y. Wang, G. Ceder, *Science.* **2022**, *378*, 1320.

[27] Y. Sun, S. Dai, *Sci. Adv.* **2021**, *7*, eabg1600.

[28] Q. F. He, J. G. Wang, H. A. Chen, Z. Y. Ding, Z. Q. Zhou, L. H. Xiong, J. H. Luan, J. M. Pelletier, J. C. Qiao, Q. Wang, L. L. Fan, Y. Ren, Q. S. Zeng, C. T. Liu, C. W. Pao, D. J. Srolovitz, Y. Yang, *Nature* **2022**, *602*, 251.

[29] S. Su Sohn, A. Kwiatkowski da Silva, Y. Ikeda, F. Körmann, W. Lu, W. Seok Choi, B. Gault, D. Ponge, J. Neugebauer, D. S. Raabe S Sohn, A. Kwiatkowski da Silva, Y. Ikeda, F. Körmann, W. Lu, B. Gault, D. Ponge, J. Neugebauer, D. Raabe, W. S. Choi, *Adv. Mater.* **2019**, *31*, 1807142.

[30] F. Wang, G. H. Balbus, S. Xu, Y. Su, J. Shin, P. F. Rottmann, K. E. Knipling, J. C. Stinville, L. H. Mills, O. N. Senkov, I. J. Beyerlein, T. M. Pollock, D. S. Gianola, *Science.* **2020**, *370*, 95.

[31] C. Lee, F. Maresca, R. Feng, Y. C. Chou, T. Ungar, M. Widom, K. An, J. D. Poplawsky, Y. C. Chou, P. K. Liaw, W. A. Curtin, *Nat. Commun.* **2021**, *12*, 6.

[32] B. Jiang, Y. Yu, J. Cui, X. Liu, L. Xie, J. Liao, Q. Zhang, Y. Huang, S. Ning, B. Jia, B. Zhu, S. Bai, L. Chen, S. J. Pennycook, J. He, *Science.* **2021**, *371*, 830.

[33] Y. Zhang, G. M. Stocks, K. Jin, C. Lu, H. Bei, B. C. Sales, L. Wang, L. K. Béland, R. E. Stoller, G. D. Samolyuk, M. Caro, A. Caro, W. J. Weber, *Nat. Commun.* **2015**, *6*, 1.

[34] C. Lu, L. Niu, N. Chen, K. Jin, T. Yang, P. Xiu, Y. Zhang, F. Gao, H. Bei, S. Shi, M.-R. R. He, I. M. Robertson, W. J. Weber, L. Wang, *Nat. Commun.* **2016**, *7*, 13564.

[35] R.-Q. Yao, Y.-T. Zhou, H. Shi, W.-B. Wan, Q.-H. Zhang, L. Gu, Y.-F. Zhu, Z. Wen, X.-Y. Lang, Q. Jiang, *Adv. Funct. Mater.* **2021**, *31*, 2009613.

[36] Z. Jia, K. Nomoto, Q. Wang, C. Kong, L. Sun, L.-C. Zhang, S.-X. Liang, J. Lu, J. J. Kruzic, *Adv. Funct. Mater.* **2021**, *31*, 2101586.

[37] Y. Zhang, X. Tian, Z. Qin, H. Jiang, *J. Magn. Magn. Mater.* **2012**, *324*, 853.

[38] B. Gludovatz, A. Hohenwarter, D. Catoor, E. H. Chang, E. P. George, R. O. Ritchie, *Science.* **2014**, *345*, 1153.

[39] K. Jin, C. Lu, L. M. Wang, J. Qu, W. J. Weber, Y. Zhang, H. Bei, *Scr. Mater.* **2016**, *119*, 65.

[40] S. Guo, C. T. Liu, *Prog. Nat. Sci. Mater. Int.* **2011**, *21*, 433.

[41] M. Z. Hossain, J. Marian, *Acta Mater.* **2014**, *80*, 107.

[42] T. Nishizawa, *Thermodynamics of Microstructures*, Asm International, **2008**.

[43] J. D. Eshelby, *Proc. R. Soc. London. Ser. A. Math. Phys. Sci.* **1957**, *241*, 376.

[44] J. D. Eshelby, *J. Appl. Phys.* **1954**, *25*, 255.

[45] Z. Wu, H. Bei, G. M. Pharr, E. P. George, *Acta Mater.* **2014**, *81*, 428.

[46] C. Varvenne, E. Clouet, *Phys. Rev. B* **2017**, *96*, 224103.

[47] D. Ma, M. Friák, J. Von Pezold, D. Raabe, J. Neugebauer, *Acta Mater.* **2015**, *85*, 53.

[48] R. L. Fleischer, *Acta Metall.* **1961**, *9*, 996.

[49] R. L. Fleischer, *Acta Metall.* **1963**, *11*, 203.

[50] R. Labusch, *Phys. status solidi* **1970**, *41*, 659.

[51] Z. Wu, Y. Gao, H. Bei, *Acta Mater.* **2016**, *120*, 108.

[52] J. D. Eshelby, in *Solid State Phys.*, Academic Press, New York, **1956**, pp. 79–144.

[53] Y. F. Ye, C. T. Liu, Y. Yang, *Acta Mater.* **2015**, *94*, 152.

[54] Y. F. Ye, X. D. Liu, S. Wang, C. T. Liu, Y. Yang, *Intermetallics* **2016**, *78*, 30.

[55] C. Varvenne, A. Luque, W. G. Nöhring, W. A. Curtin, *Phys. Rev. B* **2016**, *93*, 104201.

[56] B. Yin, S. Yoshida, N. Tsuji, W. A. Curtin, *Nat. Commun.* **2020**, *11*, 2507.

[57] B. Yin, W. A. Curtin, *npj Comput. Mater.* **2019**, *5*, 14.

[58] W. G. Nöhring, W. A. Curtin, *Scr. Mater.* **2019**, *168*, 119.

[59] C. Varvenne, A. Luque, W. A. Curtin, *Acta Mater.* **2016**, *118*, 164.

[60] C. Varvenne, G. P. M. Leyson, M. Ghazisaeidi, W. A. Curtin, *Acta Mater.* **2017**, *124*, 660.

[61] Y. Zhang, Y. J. Zhou, J. P. Lin, G. L. Chen, P. K. Liaw, *Adv. Eng. Mater.* **2008**, *10*, 534.

[62] Z. Wang, Y. Huang, Y. Yang, J. Wang, C. T. Liu, *Scr. Mater.* **2015**, *94*, 28.

[63] Q. F. He, P. H. Tang, H. A. Chen, S. Lan, J. G. Wang, J. H. Luan, M. Du, Y. Liu, C. T. Liu, C. W. Pao, Y. Yang, *Acta Mater.* **2021**, *216*, 117140.

[64] A. Fantin, G. O. Lepore, A. M. Manzoni, S. Kasatikov, T. Scherb, T. Huthwelker, F. d'Acapito, G. Schumacher, *Acta Mater.* **2020**, *193*, 329.

[65] W.-R. Jian, Z. Xie, S. Xu, Y. Su, X. Yao, I. J. Beyerlein, *Acta Mater.* **2020**, *199*, 352.

[66] Q.-J. Li, H. Sheng, E. Ma, *Nat. Commun.* **2019**, *10*, 3563.

[67] Q. Ding, Y. Zhang, X. Chen, X. Fu, D. Chen, S. Chen, L. Gu, F. Wei, H. Bei, Y. Gao, M. Wen, J. Li, Z. Zhang, T. Zhu, R. O. Ritchie, Q. Yu, *Nature* **2019**, *574*, 223.

[68] R. Zhang, S. Zhao, J. Ding, Y. Chong, T. Jia, C. Ophus, M. Asta, R. O. Ritchie, A. M. Minor, *Nature* **2020**, *581*, 283.

[69] X. Wu, *J. Mater. Sci. Technol.* **2023**, *147*, 189.

[70] Y. Wu, F. Zhang, X. Yuan, H. Huang, X. Wen, Y. Wang, M. Zhang, H. Wu, X. Liu, H. Wang, S. Jiang, Z. Lu, *J. Mater. Sci. Technol.* **2021**, *62*, 214.

[71] F. A. Lindemann, *Phys. Zeitschrift* **1910**, 609.

[72] J.-W. Yeh, S.-Y. Chang, Y.-D. Hong, S.-K. Chen, S.-J. Lin, *Mater. Chem. Phys.* **2007**, *103*, 41.

[73] L. R. Owen, N. G. Jones, *J. Mater. Res.* **2018**, *33*, 2954.

[74] W. Guo, W. Dmowski, J.-Y. Noh, P. Rack, P. K. Liaw, T. Egami, *Metall. Mater. Trans. A* **2013**, *44*, 1994.

[75] L. J. Santodonato, Y. Zhang, M. Feygenson, C. M. Parish, M. C. Gao, R. J. K. Weber, J. C. Neuefeind, Z. Tang, P. K. Liaw, *Nat. Commun.* **2015**, *6*, 5964.

[76] L. R. Owen, E. J. Pickering, H. Y. Playford, H. J. Stone, M. G. Tucker, N. G. Jones, *Acta Mater.* **2017**, *122*, 11.

[77] Y. Tong, G. Velisa, S. Zhao, W. Guo, T. Yang, K. Jin, C. Lu, H. Bei, J. Y. P. Ko, D. C. Pagan, Y. Zhang, L. Wang, F. X. Zhang, *Materialia* **2018**, *2*, 73.

[78] Y. Tong, S. Zhao, K. Jin, H. Bei, J. Y. P. Ko, Y. Zhang, F. X. Zhang, *Scr. Mater.* **2018**, *156*, 14.

[79] Y. Tong, S. Zhao, H. Bei, T. Egami, Y. Zhang, F. Zhang, *Acta Mater.* **2020**, *183*, 172.

[80] Y. Tong, K. Jin, H. Bei, J. Y. P. Ko, D. C. Pagan, Y. Zhang, F. X. Zhang, *Mater. Des.* **2018**, *155*, 1.

[81] Y. Ren, X. Zuo, *Small Methods* **2018**, *2*, 1800064.

[82] H. Diao, L. J. Santodonato, Z. Tang, T. Egami, P. K. Liaw, *JOM* **2015**, *67*, 2321.

[83] A. Mancini, L. Malavasi, *Chem. Commun.* **2015**, *51*, 16592.

[84] J. S. Chen, Y. Liu, Y. Zhai, T. X. Fan, *Sci. Rep.* **2019**, *9*, 1.

[85] N. Cherkashin, T. Denneulin, M. J. Hÿtch, *Sci. Rep.* **2017**, *7*, 1.

[86] S. Fujinaka, Y. Sato, R. Teranishi, K. Kaneko, *J. Mater. Sci.* **2020**, *55*, 8123.

[87] B. Goris, J. De Beenhouwer, A. De Backer, D. Zanaga, K. J. Batenburg, A. Sánchez-

Iglesias, L. M. Liz-Marzán, S. Van Aert, S. Bals, J. Sijbers, G. Van Tendeloo, *Nano Lett.* **2015**, *15*, 6996.

[88] J.-M. Zuo, J. Tao, in *Scanning Transm. Electron Microsc.* (Eds.: S. J. Pennycook, P. D. Nellist), Springer, New York, **2011**, pp. 393–427.

[89] Y. T. Shao, R. Yuan, H. W. Hsiao, Q. Yang, Y. Hu, J. M. Zuo, *Ultramicroscopy* **2021**, *231*, 113252.

[90] A. Kumar, J. N. Baker, P. C. Bowes, M. J. Cabral, S. Zhang, E. C. Dickey, D. L. Irving, J. M. LeBeau, *Nat. Mater.* **2021**, *20*, 62.

[91] V. B. Ozdol, C. Gammer, X. G. Jin, P. Ercius, C. Ophus, J. Ciston, A. M. Minor, *Appl. Phys. Lett.* **2015**, *106*.

[92] A. A. Oni, X. Sang, S. V. Raju, S. Dumpala, S. Broderick, A. Kumar, S. Sinnott, S. Saxena, K. Rajan, J. M. Lebeau, *Appl. Phys. Lett.* **2015**, *106*, 11601.

[93] P. Galindo, J. Pizarro, S. Molina, K. Ishizuka, *Microsc. Anal.* **2009**, 23.

[94] L. Jones, P. D. Nellist, *Microsc. Microanal.* **2013**, *19*, 1050.

[95] D. Cooper, T. Denneulin, N. Bernier, A. Béché, J. L. Rouvière, *Micron* **2016**, *80*, 145.

[96] M. J. Hÿtch, E. Snoeck, R. Kilaas, *Ultramicroscopy* **1998**, *74*, 131.

[97] X. Chen, Q. Wang, Z. Cheng, M. Zhu, H. Zhou, P. Jiang, L. Zhou, Q. Xue, F. Yuan, J. Zhu, X. Wu, E. Ma, *Nature* **2021**, *592*, 712.

[98] Y.-T. Shao, R. Yuan, Y. Hu, Q. Yang, J.-M. Zuo, *arXiv Prepr. arXiv1903.04082* **2019**.

[99] A. Béché, J. L. Rouvière, J. P. Barnes, D. Cooper, *Ultramicroscopy* **2013**, *131*, 10.

[100] G. Kim, H. Diao, C. Lee, A. T. Samaei, T. Phan, M. de Jong, K. An, D. Ma, P. K. Liaw, W. Chen, *Acta Mater.* **2019**, *181*, 124.

[101] H. S. Oh, D. Ma, G. P. Leyson, B. Grabowski, E. S. Park, F. Körmann, D. Raabe, *Entropy* **2016**, *18*.

[102] I. Toda-Caraballo, J. S. Wróbel, S. L. Dudarev, D. Nguyen-Manh, P. E. J. Rivera-Díaz-del-Castillo, *Acta Mater.* **2015**, *97*, 156.

[103] H. Song, F. Tian, Q.-M. M. Hu, L. Vitos, Y. Wang, J. Shen, N. Chen, *Phys. Rev. Mater.*

2017, *1*, 23404.

[104] N. L. Okamoto, K. Yuge, K. Tanaka, H. Inui, E. P. George, *AIP Adv.* **2016**, *6*, 125008.

[105] Y. Yang, Q. HE, *Acta Met. Sin* **2021**, *57*, 385.

[106] S. Xu, T. Odaira, S. Sato, X. Xu, T. Omori, S. Harjo, T. Kawasaki, H. Seiner, K. Zoubková, Y. Murakami, R. Kainuma, *Nat. Commun.* **2022**, *13*, 5307.

[107] J. Mohd Jani, M. Leary, A. Subic, M. A. Gibson, *Mater. Des.* **2014**, *56*, 1078.

[108] D. Wang, Y. Ji, X. Ren, Y. Wang, *Annu. Rev. Mater. Res.* **2022**, *52*, 159.

[109] Y. Wang, X. Ren, K. Otsuka, *Phys. Rev. Lett.* **2006**, *97*, 225703.

[110] X. Ren, *Phys. status solidi* **2014**, *251*, 1982.

[111] T. Saito, T. Furuta, J.-H. Hwang, S. Kuramoto, K. Nishino, N. Suzuki, R. Chen, A. Yamada, K. Ito, Y. Seno, T. Nonaka, H. Ikehata, N. Nagasako, C. Iwamoto, Y. Ikuhara, T. Sakuma, *Science.* **2003**, *300*, 464.

[112] Y. Tanaka, Y. Himuro, R. Kainuma, Y. Sutou, T. Omori, K. Ishida, *Science.* **2010**, *327*, 1488.

[113] T. Omori, K. Ando, M. Okano, X. Xu, Y. Tanaka, I. Ohnuma, R. Kainuma, K. Ishida, *Science.* **2011**, *333*, 68.

[114] J. Xia, Y. Noguchi, X. Xu, T. Odaira, Y. Kimura, M. Nagasako, T. Omori, R. Kainuma, *Science.* **2020**, *369*, 855.

[115] R. J. Talling, R. J. Dashwood, M. Jackson, D. Dye, *Acta Mater.* **2009**, *57*, 1188.

[116] S. Hao, L. Cui, F. Guo, Y. Liu, X. Shi, D. Jiang, D. E. Brown, Y. Ren, *Sci. Rep.* **2015**, *5*, 1.

[117] D. Jiang, J. An, Y. Liu, Z. Ma, F. Liu, H. Yang, X. Ren, K. Yu, J. Zhang, X. Jiang, Y. Ren, L. Cui, *Phys. Rev. B* **2021**, *104*, 24102.

[118] Y. Wang, X. Ren, K. Otsuka, A. Saxena, *Acta Mater.* **2008**, *56*, 2885.

[119] H. Wang, Q. F. He, A. D. Wang, Y. Yang, *J. Appl. Phys.* **2023**, *133*, 55105.

[120] A. V. Granato, *Phys. Rev. Lett.* **1992**, *68*, 974.

[121] C. Lee, G. Song, M. C. Gao, R. Feng, P. Chen, J. Brechtl, Y. Chen, K. An, W. Guo, J. D.

Poplawsky, S. Li, A. T. Samaei, W. Chen, A. Hu, H. Choo, P. K. Liaw, *Acta Mater.* **2018**, *160*, 158.

[122] Y. W. Song, M. Jin, S. Zuo, X. Jin, *Mater. Lett.* **2019**, *252*, 96.

[123] W. Wang, P. Luo, Y. Wei, Y. Ji, C. Liu, X. Ren, *Acta Mater.* **2022**, *231*, 117874.

[124] Michael F. Ashby, *The CES EduPack Resource Booklet 2: Material and Process Selection Charts*, Granta Design Limited, Cambridge, **2009**.

[125] J. R. Greer, J. T. M. De Hosson, *Prog. Mater. Sci.* **2011**, *56*, 654.

[126] I. Toda-Caraballo, P. E. J. J. Rivera-Díaz-del-Castillo, *Acta Mater.* **2015**, *85*, 14.

[127] I. Toda-Caraballo, *Scr. Mater.* **2017**, *127*, 113.

[128] S. I. Rao, B. Akdim, E. Antillon, C. Woodward, T. A. Parthasarathy, O. N. Senkov, *Acta Mater.* **2019**, *168*, 222.

[129] F. Maresca, W. A. Curtin, *Acta Mater.* **2020**, *182*, 144.

[130] F. Maresca, W. A. Curtin, *Acta Mater.* **2020**, *182*, 235.

[131] H. A. Moreen, R. Taggart, D. H. Polonis, *Metall. Trans.* **1971**, *2*, 265.

[132] H. Suzuki, *Dislocations in solids* **1980**, *4*, 191.

[133] A. R. Büchner, W. Wunderlich, *Phys. status solidi* **1993**, *135*, 391.

[134] C. Lee, Y. Chou, G. Kim, M. C. Gao, K. An, J. Brechtl, C. Zhang, W. Chen, J. D. Poplawsky, G. Song, Y. Ren, Y.-C. Chou, P. K. Liaw, *Adv. Mater.* **2020**, *32*, 2004029.

[135] P.Shewmon, *Diffusion in Solids*, Springer Cham, **1979**.

[136] K. Y. Tsai, M. H. Tsai, J. W. Yeh, *Acta Mater.* **2013**, *61*, 4887.

[137] S. Zhao, *J. Mater. Sci. Technol.* **2020**, *44*, 133.

[138] Y. P. Zhao, Y. K. Dou, X. F. He, H. Q. Deng, L. F. Wang, W. Yang, *Comput. Mater. Sci.* **2023**, *218*, 111943.

[139] J. Zhang, C. Gadelmeier, S. Sen, R. Wang, X. Zhang, Y. Zhong, U. Glatzel, B. Grabowski, G. Wilde, S. V. Divinski, *Acta Mater.* **2022**, *233*, 117970.

[140] S. Sen, X. Zhang, L. Rogal, G. Wilde, B. Grabowski, S. V. Divinski, *Scr. Mater.* **2023**, *224*, 115117.

[141] K. Jin, H. Bei, *Front. Mater.* **2018**, *5*, 26.

[142] Z. Fan, H. Wang, Y. Wu, X. J. Liu, Z. P. Lu, *RSC Adv.* **2016**, *6*, 52164.

[143] Z. Sun, C. Shi, L. Gao, S. Lin, W. Li, *J. Alloys Compd.* **2022**, *901*, 163554.

[144] P.-C. Wei, C.-N. Liao, H.-J. Wu, D. Yang, J. He, G. V Biesold-McGee, S. Liang, W.-T. Yen, X. Tang, J.-W. Yeh, Z. Lin, J.-H. He, *Adv. Mater.* **2020**, *32*, 1906457.

[145] B. Abeles, *Phys. Rev.* **1963**, *131*, 1906.

[146] J. Yang, G. P. Meisner, L. Chen, *Appl. Phys. Lett.* **2004**, *85*, 1140.

[147] L. Hu, Y. Zhang, H. Wu, J. Li, Y. Li, M. Mckenna, J. He, F. Liu, S. J. Pennycook, X. Zeng, *Adv. Energy Mater.* **2018**, *8*, 1802116.

[148] B. Jiang, Y. Yu, H. Chen, J. Cui, X. Liu, L. Xie, J. He, *Nat. Commun.* **2021**, *12*, 3234.

[149] B. Jiang, W. Wang, S. Liu, Y. Wang, C. Wang, Y. Chen, L. Xie, M. Huang, J. He, *Science.* **2022**, *377*, 208.

[150] X. Qian, J. Zhou, G. Chen, *Nat. Mater.* **2021**, *20*, 1188.

[151] N. F. Shkodich, K. V Kuskov, A. S. Sedegov, I. D. Kovalev, A. V Panteleeva, Y. S. Vergunova, Y. B. Scheck, E. Panina, N. Stepanov, I. Serhiienko, D. Moskovskikh, *J. Alloys Compd.* **2022**, *893*, 162030.

[152] O. Madelung, P. G. Klemens, G. Neuer, G. K. White, B. Sundqvist, C. Uher, *Thermal Conductivity of Pure Metals and Alloys*, Springer, Berlin, **1991**.

[153] Z. Zhang, D. E. J. Armstrong, P. S. Grant, *Prog. Mater. Sci.* **2022**, *123*, 100807.

[154] S. Zhao, T. Egami, G. M. Stocks, Y. Zhang, *Phys. Rev. Mater.* **2018**, *2*, 13602.

[155] B. N. Singh, A. J. E. Foreman, *Philos. Mag. A* **1992**, *66*, 975.

[156] A. J. E. Foreman, W. J. Phythian, C. A. English, *Philos. Mag. A* **1992**, *66*, 671.

[157] Y. Chen, S. Wang, H. Feng, W. Li, B. Liu, J. Li, Y. Liu, P. K. Liaw, Q. Fang, *Int. J. Plast.* **2023**, *162*, 103497.

[158] Y. Su, S. Xia, J. Huang, Q. Liu, H. Liu, C. Wang, Y. Wang, *Metals.* **2021**, *11*, DOI 10.3390/met11050706.

[159] Y. Zong, N. Hashimoto, H. Oka, *Nucl. Mater. Energy* **2022**, *31*, 101158.

[160] M. Sadeghilaridjani, A. Ayyagari, S. Muskeri, V. Hasannaeimi, R. Salloom, W.-Y. Chen, S. Mukherjee, *J. Nucl. Mater.* **2020**, *529*, 151955.

[161] Y. Lu, H. Huang, X. Gao, C. Ren, J. Gao, H. Zhang, S. Zheng, Q. Jin, Y. Zhao, C. Lu, T. Wang, T. Li, *J. Mater. Sci. Technol.* **2019**, *35*, 369.

[162] O. El-Atwani, N. Li, M. Li, A. Devaraj, J. K. S. Baldwin, M. M. Schneider, D. Sobieraj, J. S. Wróbel, D. Nguyen-Manh, S. A. Maloy, E. Martinez, *Sci. Adv.* **2019**, *5*, eaav2002.

[163] M. Luo, S. Guo, *Nat. Rev. Mater.* **2017**, *2*, 17059.

[164] B. You, M. T. Tang, C. Tsai, F. Abild-Pedersen, X. Zheng, H. Li, *Adv. Mater.* **2019**, *31*, 1.

[165] S. Schnur, A. Groß, *Phys. Rev. B* **2010**, *81*, 033402.

[166] Y. Xin, S. Li, Y. Qian, W. Zhu, H. Yuan, P. Jiang, R. Guo, L. Wang, *ACS Catal.* **2020**, *10*, 11280.

[167] T. Ling, D. Y. Yan, H. Wang, Y. Jiao, Z. Hu, Y. Zheng, L. Zheng, J. Mao, H. Liu, X. W. Du, M. Jaroniec, S. Z. Qiao, *Nat. Commun.* **2017**, *8*, 1.

[168] H. J. Qiu, G. Fang, Y. Wen, P. Liu, G. Xie, X. Liu, S. Sun, *J. Mater. Chem. A* **2019**, *7*, 6499.

[169] X. Cui, B. Zhang, C. Zeng, S. Guo, *MRS Commun.* **2018**, *8*, 1230.

[170] Z. Jin, J. Lv, H. Jia, W. Liu, H. Li, Z. Chen, X. Lin, G. Xie, X. Liu, S. Sun, H. J. Qiu, *Small* **2019**, *15*, 1904180.

[171] T. A. A. Batchelor, J. K. Pedersen, S. H. Winther, I. E. Castelli, K. W. Jacobsen, J. Rossmeisl, *Joule* **2019**, *3*, 834.

[172] Z. Y. Lv, X. J. Liu, B. Jia, H. Wang, Y. Wu, Z. P. Lu, *Sci. Rep.* **2016**, *6*, 1.

[173] S. Nellaiappan, N. K. Katiyar, R. Kumar, A. Parui, K. D. Malviya, K. G. Pradeep, A. K. Singh, S. Sharma, C. S. Tiwary, K. Biswas, *ACS Catal.* **2020**, *10*, 3658.

[174] Y. Sun, W. Zhang, Q. Zhang, Y. Li, L. Gu, S. Guo, *Matter* **2023**, *6*, 193.

[175] Z. Ding, J. Bian, S. Shuang, X. Liu, Y. Hu, C. Sun, Y. Yang, *Adv. Sustain. Syst.* **2020**, *4*, 1.

[176] A. A. H. Tajuddin, M. Wakisaka, T. Ohto, Y. Yu, H. Fukushima, H. Tanimoto, X. Li, Y. Misu, S. Jeong, J. Fujita, H. Tada, T. Fujita, M. Takeguchi, K. Takano, K. Matsuoka, Y. Sato, Y. Ito, *Adv. Mater.* **2023**, *35*, 2207466.

[177] Z. Jia, T. Yang, L. Sun, Y. Zhao, W. Li, J. Luan, F. Lyu, L.-C. Zhang, J. J. Kruzic, J.-J. Kai, J. C. Huang, J. Lu, C. Tsuan Liu, *Adv. Mater.* **2020**, *32*, 2000385.

[178] R. Li, X. Liu, W. Liu, Z. Li, K. C. Chan, Z. Lu, *Adv. Sci.* **2022**, *9*, 1.

[179] R. Song, J. Han, M. Okugawa, R. Belosludov, T. Wada, J. Jiang, D. Wei, A. Kudo, Y. Tian, M. Chen, H. Kato, *Nat. Commun. 2022 131* **2022**, *13*, 1.

[180] T. Yang, Y. L. Zhao, Y. Tong, Z. B. Jiao, J. Wei, J. X. Cai, X. D. Han, D. Chen, A. Hu, J. J. Kai, K. Lu, Y. Liu, C. T. Liu, *Science.* **2018**, *362*, 933.

[181] W. H. Liu, Z. P. Lu, J. Y. He, J. H. Luan, Z. J. Wang, B. Liu, Y. Liu, M. W. Chen, C. T. Liu, *Acta Mater.* **2016**, *116*, 332.

[182] M.-H. Tsai, R.-C. Tsai, T. Chang, W.-F. Huang, *Metals.* **2019**, *9*.

[183] Z. Zhou, Y. Zhou, Q. He, Z. Ding, F. Li, Y. Yang, *npj Comput. Mater.* **2019**, *5*, 1.

[184] J. Huang, W. Fang, C. Xue, T. Peng, H. Yu, J. Li, L. Sun, X. He, B. Liu, Y. Yang, F. Yin, *Comput. Mater. Sci.* **2023**, *221*, 112089.

[185] C. Tandoc, Y. J. Hu, L. Qi, P. K. Liaw, *npj Comput. Mater.* **2023**, *9*, 1.